International Journal of Solids and Structures 309 (2025) 113162

Contents lists available at ScienceDirect

International Journal of Solids and Structures

journal homepage: www.elsevier.com/locate/ijsolstr

A numerical study on the physical couplings of a geometrically linear thermo-chemo-mechanical model

Johannes Gisy, Alexander Dyck, Thomas Böhlke *

Institute of Engineering Mechanics, Chair for Continuum Mechanics, Karlsruhe Institute of Technology (KIT), Kaiserstraße 10, 76131, Karlsruhe, Germany

ARTICLE INFO

Keywords:
Coupled problems
Thermo-chemo-mechanical model
Continuum thermodynamics
Finite element method

ABSTRACT

Physically coupled models are used in various research fields to solve problems concerning the interaction of solid materials with thermal, chemical or electrical boundary conditions. If beside the mechanical fields two or more additional fields (e.g. temperature and concentration) have to be taken into account, the determination of the impact on the mechanical fields (e.g. stress and yield strength) and the influence of the boundary conditions leads to an ambitious task. To deal with this issue, a thermo-chemo-mechanical model using a geometrically linear theory and a thermodynamically consistent derivation, is presented. The model is specified for linear elastic isotropic solid materials. A fully coupled set of partial differential equations is obtained. A Finite Element implementation using the User Element subroutine of ABAQUS is performed. A detailed description about the steps necessary to derive the corresponding element formulation is provided, thereby supporting the development of user-defined elements. The user-defined element is used for a series of simulations involving submodels with up to seven different combinations of active fields including thermo-chemical, thermo-mechanical and chemo-mechanical couplings. Three sets of boundary conditions are considered, leading to closed and open systems. This procedure, which is exemplified in one- and three-dimensional examples, enlightens strong and weak couplings and outlines the mechanical role on the interaction between the solid material and the chemical environment. Additionally, the implications of a geometrical linearization on the interpretation of the concentration is illustrated.

1. Introduction

Motivation. Multi-field models consisting of more than two fields, lead to coupled partial differential equations which challenge the prediction of the constitutive response. In thermo-chemo-mechanical multi-field models, the chemical and mechanical states are strongly dependent on all fields, thus, the actual stress state as well as the chemical potential driving the diffusion of species, are highly nonlinear quantities. In order to provide a reliable coupled continuum model, an exploration on the different couplings involved and on their contributions to the constitutive response, clarifying the suitability of such a coupled model, is needed.

State of the art. In different research fields, such as solidification, oxidation, electric energy storage and so forth, coupled multi-field problems seek for suitable continuum models. In the past decades, the following models among others have been developed. In Bower et al. (2011) an electro-chemo-mechanical model using a geometrically nonlinear theory is presented to study the lithium diffusion within a lithium-ion half cell. In comparison to a Fick-type diffusion, Anand (2012) suggests a chemo-mechanical model using a geometrically nonlinear theory with diffusion of Cahn-Hilliard type. In Di Leo et al. (2015) the coupling between the electro-chemical performance and plasticity is studied proposing a chemo-mechanical model using a geometrically nonlinear theory. The phase transition that occurs between the diffusive species and the host material is of interest in Afshar and Di Leo (2021) presenting a chemo-mechanical gradient model using a geometrically nonlinear theory. The coupling is extended by a damage variable in Bistri and Di Leo (2023) proposing an electro-chemo-mechanical gradient model using a geometrically nonlinear theory to study fracture evolution within electrodes of all-solid-state batteries.

While the electro-chemical coupling is of main interest to study performance and structural stability of electrodes, thermo-chemical coupled models aim at solid materials incorporating diffusive processes. The general thermodynamics of thermo-chemo-mechanical models are established since the last century (cf. Meixner and Reik, 1959; de Groot and Mazur, 1984; Müller, 1985; Greve, 2003) based on the framework of mixture theory. A review on the evolution of the thermo-chemical coupling with respect to modeling and experimental sights is found in Rahman and Saghir (2014). In Johlitz and Lion (2013), Lion

* Corresponding author.
E-mail address: thomas.boehlke@kit.edu (T. Böhlke).

https://doi.org/10.1016/j.ijsolstr.2024.113162
Received 11 June 2024; Received in revised form 31 October 2024; Accepted 25 November 2024
Available online 11 December 2024

and Johlitz (2020) and Anguiano et al. (2022) the development of thermo-chemo-mechanical models is based on the principles of mixture theory. Gurtin and Vargas (1971) reinterpret the heat and entropy fluxes, though identical results are obtained. A framework for diffusive species within a solid host material following this reinterpretation is collected in Gurtin et al. (2010).

In Oskay and Haney (2010) a thermo-chemo-mechanical model using a geometrically nonlinear theory is presented to study the oxidation of titanium. The formation of thermal barrier coatings is of interest in Loeffel and Anand (2011) proposing a thermo-chemo-mechanically coupled model using a geometrically nonlinear theory. A multiscale approach for modeling oxidation of titanium is presented in Oskay (2012) suggesting thermo-chemo-mechanical coupling. Another approach using a different formulation for deriving driving forces is suggested by Qin and Zhong (2021).

Objective of the work and originality. The present work uses a thermo-chemo-mechanical multi-field model to study numerically the involved couplings as well as their contribution to the mechanical stress state and the chemical diffusion state. The exploration clarifies the role of the different fields on the resultant material response providing a first step of predicting the material state on the basis of a series of Finite Element simulations.

Based on the work of Anand (2011), a solid host material exposed to a diffusive species under nonisothermal conditions is considered. The choice of a geometrically linear theory follows the goal to study the nature of coupling effects within the constitutive theory proposed by Anand (2011), who specified the constitutive theory assuming small strains only. The balance equations involve an extended energy balance following the previous mentioned work of Gurtin and Vargas (1971). Thus, the model is thermodynamically consistent according to standard formulations introduced by Coleman and Gurtin (1967) in classical irreversible thermodynamics. The specific free energy function is extended to account for larger concentrations as well as to obtain a constant specific heat capacity at constant volume. This is achieved by adopting a chemo-mechanical formulation introduced in Anand and Govindjee (2020) with a thermo-mechanical formulation proposed by Neumann and Böhlke (2016). This work focuses on the following topics:

- The different couplings of the thermo-chemo-mechanical model are studied numerically. The exploration elucidates the role of all fields on the mechanical stress state as well as on the state of the chemical potential driving the diffusion of species for a specified set of material parameters. The study is built up on one-dimensional Finite Element simulations, though, their propositions are obtained in a more complex example as well.
- The development of a user-defined element using a User Element (UEL) subroutine provided by ABAQUS is highlighted. The procedure of discretization of the field equations is presented and the analytical derivation of the residuals together with their corresponding element tangents is depicted. Further, remarks on the usage of user-defined elements are provided to create a reliable workflow.

Outline. This work begins with the development of the thermo-chemo-mechanical model stating the balance equations followed by the exploitation of the second law of thermodynamics using the Coleman-Noll procedure and the introduction of constitutive assumptions leading to a set of partial differential equations. The subsequent section contains comments on the Finite Element implementation. The element tangents as well as all expressions needed are provided in the appendix. In the next section, the couplings within the multi-field model are studied, followed by a full-field problem supporting the result of the preceding study. After this problem, the results of this work are concluded.

Notation. First order tensors are denoted by bold lowercase latin letters, i.e. $\boldsymbol{k}$, while second order tensors use either bold capital latin letters or bold greek letters, i.e. $\boldsymbol{K}, \boldsymbol{\sigma}$. Third order and fourth order tensors use blackboard lowercase and capital latin letters $\Bbbk$ and $\mathbb{K}$, respectively. The operator $\mathrm{sym}(\boldsymbol{K})$ returns the symmetric part of $\boldsymbol{K}$. The trace of a second order tensor is indicated by $\mathrm{tr}(\boldsymbol{K})$. Spherical and the deviatoric parts of second order tensors are denoted by $\boldsymbol{K}^{\circ}$ and $\boldsymbol{K}'$, respectively. The scalar product and the dyadic product are expressed with $(\bullet)\cdot(\bullet)$ and $(\bullet)\otimes(\bullet)$, respectively. A linear mapping of a tensor is indicated by a bracket $[\bullet]$, e.g. $a_i = k_{ijm}A_{jm}$ and $A_{ij} = K_{ijmn}B_{mn}$ for third and fourth order operators in case of Cartesian coordinates. The material time derivative is denoted by dot, e.g. $\dot{\boldsymbol{a}}$. The differential operators $\mathrm{grad}(\boldsymbol{k})$ and $\mathrm{div}(\boldsymbol{k})$ are the gradient and the divergence with respect to the current placement. Column vectors are indicated by letters underlined once $\underline{(\bullet)}$. Capital letters denoting matrices are underlined twice $\underline{\underline{K}}$.

2. Development of the coupled continuum model

2.1. Balance equations

Predefined assumptions. The model takes into account a solid host material exposed to a diffusing species and undergoing a deformation process at nonisothermal conditions. The basic fields are the displacement $\boldsymbol{u}(\boldsymbol{x},t)$, the (absolute) temperature $\theta(\boldsymbol{x},t)$ and concentration $c(\boldsymbol{x},t)$. These fields depend on the current placement of a material point $\boldsymbol{x}$. The reference placement of a material point for $t=0$ is denoted by $\boldsymbol{X}$. In case of a geometrically linear theory, the deformations are assumed to be small such that $|\boldsymbol{H}| \ll 1$ with $\boldsymbol{H} = \partial\boldsymbol{u}/\partial\boldsymbol{X} \approx \partial\boldsymbol{u}/\partial\boldsymbol{x}$ is valid. The linear strain is defined by $\boldsymbol{\varepsilon} = \mathrm{sym}(\boldsymbol{H})$. Balance equations are formulated for regular points in the current placement such that cracks are excluded and a continuous transplacement between the current placement and the reference placement exists. The control volume V is assumed to coincide with the space occupied by the solid material.

The terms "density" and "specific" denote quantities per unit volume and quantities per unit mass, respectively. A distinction between the volume in the current placement and the initial placement is omitted due to the previous assumptions.

Balance of mass. The overall mass balance for the mixture of solid material and diffusing species reads

$$\dot{\rho}_{\mathrm{M}} + \rho_{\mathrm{M}}\mathrm{div}(\boldsymbol{v}) = 0 \tag{1}$$

with $\boldsymbol{v} = \dot{\boldsymbol{u}}$ denoting the velocity of a material point of the solid material. For the mass density of the mixture follows $\rho_{\mathrm{M}} \approx \rho_{\mathrm{M},0}$, due to $|\boldsymbol{H}| \ll 1$, with the index 0 denoting the mass density in the reference placement. The mass density of the mixture is assembled additively with the mass density ρ_{S} of the solid material and the mass density of the diffusing species ρ_{D}, reading

$$\rho_{\mathrm{M}} = \rho_{\mathrm{S}} + \rho_{\mathrm{D}}. \tag{2}$$

In the following, combinations of host materials with diffusing species are considered for which $\rho_{\mathrm{D}} \ll \rho_{\mathrm{S}}$ can be assumed, such that $\rho_{\mathrm{M}} \approx \rho_{\mathrm{S}}$ is valid. The mass density of the diffusing species is represented as a molar density $\rho_{\mathrm{D}} = Mc$ in moles of diffusing species per unit volume with M denoting the molar mass of the diffusing species. At regular points, the local balance of diffusing species reads

$$\dot{c} = -\mathrm{div}(\boldsymbol{j}). \tag{3}$$

A flux of diffusing species $\boldsymbol{j}$ pointing inwards the volume is introduced (Fried and Gurtin, 1999). For convenience, the mass density of mixture is denoted by ρ omitting additional indexing.

Balance of linear momentum. The quasi-static balance of linear momentum for the mixture is

$$\boldsymbol{0} = \mathrm{div}(\boldsymbol{\sigma}) + \rho\boldsymbol{b}. \tag{4}$$

This formulation neglects any inertia as wave propagation within the solid is considerably faster than species diffusion (cf. Gurtin et al., 2010). The Cauchy stress tensor is denoted by $\boldsymbol{\sigma}$. Specific body forces are represented by $\boldsymbol{b}$.

Balance of angular momentum. Considering Boltzman continua within this model, the balance of angular momentum states $\boldsymbol{\sigma} = \boldsymbol{\sigma}^{\mathsf{T}}$.

Balance of energy. The integral balance of energy of the mixture reads

$$\frac{\mathrm{d}}{\mathrm{d}t}\int_{\mathrm{V}} \rho e \,\mathrm{d}v = \int_{\partial \mathrm{V}} \boldsymbol{\sigma}^{\mathsf{T}}\boldsymbol{v}\cdot\,\mathrm{d}\boldsymbol{a} + \int_{\mathrm{V}} \boldsymbol{v}\cdot\rho\boldsymbol{b}\,\mathrm{d}v - \int_{\partial \mathrm{V}} \boldsymbol{q}\cdot\,\mathrm{d}\boldsymbol{a} + \int_{\mathrm{V}} \rho w\,\mathrm{d}v - \int_{\partial \mathrm{V}} \mu\boldsymbol{j}\cdot\,\mathrm{d}\boldsymbol{a}. \tag{5}$$

On the left side of Eq. (5), the kinetic energy is neglected in accordance with the vanishing inertia terms in Eq. (4). The energy of the mixture is given by its specific internal energy e. The first two terms on the right side of Eq. (5) describe the standard mechanical contributions. The third and fourth terms are the heat flux $\boldsymbol{q}$ and the specific heat supply w, respectively. The last term denotes an energy flux due to the energy per moles of diffusing species μ which is transported into the mixture by the flux of diffusing species (cf. Gurtin et al., 2010). The local formulation of Eq. (5) is obtained after the following steps: The divergence theorem is used to transform the surface integrals into volume integrals. Equation (1) eliminates the balance of mass on the left-hand side and Eq. (3) substitutes $\operatorname{div}(\boldsymbol{j})$ on the right-hand side. Equation (4) removes the mechanical energy contributions. The local representation reads

$$\rho\dot{e} = \boldsymbol{\sigma}\cdot\dot{\boldsymbol{\varepsilon}} - \operatorname{div}(\boldsymbol{q}) + \rho w + \mu\dot{c} - \operatorname{grad}(\mu)\cdot\boldsymbol{j}. \tag{6}$$

Balance of entropy. The balance of entropy is introduced such that the entropy flux is considered as $\boldsymbol{q}/\theta$ and the specific entropy supply is w/θ (cf. Coleman and Gurtin, 1967). The choice of such an entropy flux is motivated in Meixner and Reik (1959) due to linearity between the heat flux, the flux of diffusing species and the entropy flux. In Gurtin and Vargas (1971) the flux of diffusing species is discussed either to be a contribution to the energy flux or to the entropy flux. For a simple material both interpretations are equivalent. The local formulation of the entropy balance, thus, reads

$$\rho\dot{\eta} = -\operatorname{div}\left(\frac{\boldsymbol{q}}{\theta}\right) + \rho\frac{w}{\theta} + p_{\eta} \tag{7}$$

where η is the specific entropy. The balance of entropy includes the entropy production p_{η}, the non-negativity of which represents the second law of thermodynamics. This introduction of the entropy balance is taken from Gurtin et al. (2010) and is used as well in Anand (2011) and Chester et al. (2015). Nevertheless, there are other approaches in mixture theory where the flux of diffusing species contributes the entropy flux (cf. Müller, 1985; Johlitz and Lion, 2013).

2.2. Implications of the Coleman-Noll procedure

The Coleman-Noll procedure (Coleman and Noll, 1963) is used to obtain necessary and sufficient restrictions for the constitutive relations. The specific internal energy is Legendre transformed by the specific free energy $\psi = e - \eta\theta$ and substituted in

$$\frac{\boldsymbol{\sigma}}{\rho}\cdot\dot{\boldsymbol{\varepsilon}} - \eta\dot{\theta} + \frac{\mu}{\rho}\dot{c} - \dot{\psi} - \frac{\boldsymbol{q}}{\rho}\cdot\frac{\boldsymbol{g}}{\theta} - \frac{\boldsymbol{j}}{\rho}\cdot\boldsymbol{m} = \frac{p_{\eta}}{\rho}\theta \geq 0. \tag{8}$$

Equation (8) is derived from the balance of entropy Eq. (7) where the specific heat source is eliminated by the balance of energy in Eq. (6) and the non-negative entropy production is required. The abbreviation $\boldsymbol{m} = \operatorname{grad}(\mu)$ is introduced. The unknown fields in Eq. (8) are

$$\mathcal{A} = \{\psi, \eta, \boldsymbol{\sigma}, \boldsymbol{q}, \boldsymbol{j}, \mu\}. \tag{9}$$

These output quantities are considered to be depending on the following input quantities

$$\mathcal{E} = \{\boldsymbol{\varepsilon}, \mathbb{k}, \theta, \boldsymbol{g}, c, \boldsymbol{f}\}. \tag{10}$$

Due to objectivity, the constitutive quantities in Eq. (9) cannot depend on the displacement, but only on the symmetric part of the displacement gradient. In addition, the gradient of the strain $\mathbb{k} = \operatorname{grad}(\boldsymbol{\varepsilon})$, the temperature gradient $\boldsymbol{g} = \operatorname{grad}(\theta)$ and the gradient of the concentration $\boldsymbol{f} = \operatorname{grad}(c)$ are used. The strain gradient and the concentration gradient are considered as both, the chemical potential and its gradient, appear in Eq. (8). If the chemical potential depends at least on strain, temperature and concentration, the flux of diffusing species has the corresponding gradients as driving forces. Thus, with respect to the principle of equipresence, the input quantities in Eq. (10) are considered for every constitutive quantity in Eq. (9). Expressing the rate of the free energy in terms of the considered input quantities in Eq. (10), the nonzero relations

$$\frac{\partial\psi}{\partial\boldsymbol{\varepsilon}} = \frac{\boldsymbol{\sigma}}{\rho}, \quad \frac{\partial\psi}{\partial\theta} = -\eta \quad \text{and} \quad \frac{\partial\psi}{\partial c} = \frac{\mu}{\rho} \tag{11}$$

are obtained. These relations are necessary to obtain thermodynamically consistent formulations. The relations in Eq. (11) are also known as state relations acknowledging the dependency on the current state (Anand, 2011) or potential relations in a more mathematical sense highlighting the role of the specific free energy as a potential. The specific free energy depends on $\boldsymbol{\varepsilon}$, θ and c, but not on the corresponding gradients. The heat flux and the flux of diffusing species contribute to the dissipation D according to

$$D = -\frac{\boldsymbol{q}}{\rho}\cdot\frac{\boldsymbol{g}}{\theta} - \frac{\boldsymbol{j}}{\rho}\cdot\boldsymbol{m} \geq 0. \tag{12}$$

For convenience, the gradient of the chemical potential in Eq. (12) is not expressed in terms of the input quantities. Rewriting the gradient of the chemical potential leads to

$$\boldsymbol{m} = \mathbb{k}\left[\frac{\partial\mu}{\partial\boldsymbol{\varepsilon}}\right] + \frac{\partial\mu}{\partial\theta}\boldsymbol{g} + \frac{\partial\mu}{\partial c}\boldsymbol{f}. \tag{13}$$

Taking Eq. (5), the Legendre transformation between the internal energy and the free energy, and using the potential relation in Eq. (11) regarding the entropy, the following expression

$$\rho c_{\varepsilon}\dot{\theta} = \theta\frac{\partial\boldsymbol{\sigma}}{\partial\theta}\cdot\dot{\boldsymbol{\varepsilon}} + \theta\frac{\partial\mu}{\partial\theta}\dot{c} + \rho w - \operatorname{div}(\boldsymbol{q}) - \boldsymbol{m}\cdot\boldsymbol{j} \tag{14}$$

represents the equation of heat conduction with the heat capacity defined by

$$c_{\varepsilon} = -\theta\frac{\partial^2\psi}{\partial\theta^2}. \tag{15}$$

So far, the introduced assumptions lead to an equivalent model as presented in Anand (2011), however, a distinction between the volume in both placements is omitted due to the geometrical linearization.

2.3. Constitutive modeling

Decomposition of the strain. The total strain is decomposed additively into three parts

$$\boldsymbol{\varepsilon} = \boldsymbol{\varepsilon}_{\mathrm{e}} + \boldsymbol{\varepsilon}_{\theta} + \boldsymbol{\varepsilon}_{\mathrm{c}}. \tag{16}$$

The first part of the strain $\boldsymbol{\varepsilon}_{\mathrm{e}}$ describes elastic deformations due to stress. The second part $\boldsymbol{\varepsilon}_{\theta}$ describes deformations due to thermal expansion reading

$$\boldsymbol{\varepsilon}_{\theta} = \boldsymbol{\alpha}\Delta\theta. \tag{17}$$

The thermal expansion tensor $\boldsymbol{\alpha}$ is assumed to be constant and in general anisotropic. A linear dependency on the temperature difference $\Delta\theta$ with a reference temperature value θ_0 is considered. The third part $\boldsymbol{\varepsilon}_{\mathrm{c}}$ describes chemical expansion and follows the ansatz

$$\boldsymbol{\varepsilon}_{\mathrm{c}} = \boldsymbol{\Omega}\Delta c \tag{18}$$

with the chemical expansion tensor $\boldsymbol{\Omega}$ describing the volume change by one mole of diffusing species within the solid host material. The chemical expansion tensor is assumed constant and in general anisotropic. Following the linear approach in the thermal strain, the chemical strain depends linearly on Δc with respect to a reference concentration c_0 as well.

Free energy. According to Eq. (11), the Cauchy stress follows from a specific free energy. Assuming Hooke's law to be valid, the relation

$$\boldsymbol{\sigma} = \rho \frac{\partial \psi}{\partial \boldsymbol{\varepsilon}} = \mathbb{C}\left[\boldsymbol{\varepsilon} - \boldsymbol{\varepsilon}_\theta - \boldsymbol{\varepsilon}_\mathrm{c}\right] \tag{19}$$

holds. The material stiffness tensor is assumed to be constant and in general anisotropic. Integration of Eq. (19) with respect to a stress-free state leads to a specific free energy of the following structure:

$$\psi(\boldsymbol{\varepsilon}, \theta, c) = \psi_\mathrm{e}(\boldsymbol{\varepsilon}, \theta, c) + \psi_{\theta\mathrm{c}}(\theta, c)\,. \tag{20}$$

The first part $\psi_\mathrm{e}(\boldsymbol{\varepsilon}, \theta, c)$ is obtained due to Eq. (19) by

$$\psi_\mathrm{e}(\boldsymbol{\varepsilon}, \theta, c) = \frac{1}{2\rho}\left(\boldsymbol{\varepsilon} - \boldsymbol{\varepsilon}_\theta - \boldsymbol{\varepsilon}_\mathrm{c}\right) \cdot \mathbb{C}\left[\boldsymbol{\varepsilon} - \boldsymbol{\varepsilon}_\theta - \boldsymbol{\varepsilon}_\mathrm{c}\right]. \tag{21}$$

The second part is assumed to have the following structure such that there is a coupled contribution, but also separate contributions from each individual field, reading

$$\psi_{\theta\mathrm{c}}(\theta, c) = \psi_\mathrm{mix}(\theta, c) + \psi_\theta(\theta) + \psi_\mathrm{c}(c)\,. \tag{22}$$

The entropic contribution $\psi_\mathrm{mix}(\theta, c)$ assumes the mixing of an ideal solid solution (DeHoff, 2006) reading

$$\psi_\mathrm{mix}(\theta, c) = \frac{R\theta c_\mathrm{max}}{\rho}\Big(c_\mathrm{n} \ln\left(c_\mathrm{n}\right) + \left(1 - c_\mathrm{n}\right) \ln\left(1 - c_\mathrm{n}\right)\Big). \tag{23}$$

A normalized concentration c_n is introduced with

$$c_\mathrm{n} = \frac{c}{c_\mathrm{max}} \tag{24}$$

relating the current concentration to a maximum concentration c_max. In literature dealing with hydrogen embrittlement, this normalized concentration refers to the occupancy (cf. Di Leo and Anand, 2013). The entropic contribution is at its highest for $c_\mathrm{n} = 0.5$ and close to zero for $c_\mathrm{n} \in \{0, 1\}$. The intensity of this entropic contribution involves the molar gas constant R, and it increases linearly regarding the temperature. The thermal contribution

$$\psi_\theta(\theta) = c_{\varepsilon,0}\left(\Delta\theta - \theta \ln\left(\frac{\theta}{\theta_0}\right)\right) - \frac{1}{2\rho}\boldsymbol{\varepsilon}_\theta \cdot \mathbb{C}\left[\boldsymbol{\varepsilon}_\theta\right] \tag{25}$$

is taken from Neumann and Böhlke (2016) leading to a constant heat capacity $c_\varepsilon = c_{\varepsilon,0}$. The chemical contribution reads

$$\psi_\mathrm{c}(c) = \frac{\widetilde{\mu}}{\rho}\Delta c \tag{26}$$

representing an energetic chemical contribution with a constant reference chemical potential $\widetilde{\mu}$.

This choice for the specific free energy is different to Anand (2011), but these changes follow precise assumptions leading to overall constant coefficients.

Sufficient thermodynamic conditions. The reduced dissipation inequality in Eq. (12) deals with the heat flux and the flux of diffusing species, respectively. Neglecting cross-coupling effects thereby following Anand (2011), the usage of Fourier's law

$$\boldsymbol{q} = -\boldsymbol{\kappa}(\mathcal{E})\,\boldsymbol{g} \tag{27}$$

with the positive semidefinite heat conductivity tensor $\boldsymbol{\kappa}$ is sufficient to obtain a non-negative thermal dissipation. In general, the heat conductivity tensor can be anisotropic. The flux of diffusing species is modeled using a Fick-type relation

$$\boldsymbol{j} = -\boldsymbol{M}(\mathcal{E})\,\boldsymbol{m} \tag{28}$$

with the positive semidefinite mobility tensor $\boldsymbol{M}$ depending on temperature and concentration which can be anisotropic in general.

Isotropic material behavior. In a first attempt, isotropic materials are considered which leads to the following material coefficients

$$\boldsymbol{\alpha} = \alpha_0 \boldsymbol{I} \qquad \boldsymbol{\Omega} = \frac{\Omega_0}{3}\boldsymbol{I} \tag{29}$$

for the strain formulations. The factor of one third in chemical expansion tensor connects the relative volume change due to species transport to the scalar molar volume, reading

$$\mathrm{tr}\left(\boldsymbol{\varepsilon}_\mathrm{c}\right) = \Omega_0 \Delta c. \tag{30}$$

The scalar thermal expansion coefficient is α_0. The isotropic material stiffness tensor is

$$\mathbb{C} = 3K_0\mathbb{P}_1 + 2G_0\mathbb{P}_2 \tag{31}$$

with the constant bulk modulus K_0 and the constant shear modulus G_0. The tensors $\mathbb{P}_1$ and $\mathbb{P}_2$ are the fourth order identity tensors for spherical tensors of second order and for symmetric deviatoric tensors of second order, respectively.

The heat conductivity tensor uses the isotropic approach

$$\boldsymbol{\kappa}(\mathcal{E}) = \kappa_0 \boldsymbol{I} \tag{32}$$

with the scalar heat conductivity κ_0. The isotropic mobility tensor is

$$\boldsymbol{M}(\mathcal{E}) = m(\theta, c)\,\boldsymbol{I} = \frac{D_0}{R\theta} c\left(1 - c_\mathrm{n}\right)\boldsymbol{I} \tag{33}$$

with the scalar mobility m which is determined by the constant diffusion coefficient D_0 and the molar gas constant R. For normalized concentrations around zero and one, the mobility vanishes. In the special case of isothermal conditions in a rigid body, this approach simplifies to Fick's law.

Necessary thermodynamic conditions. For isotropic materials, Hooke's law in Eq. (19) leads to

$$\boldsymbol{\sigma} = 3K_0\left(\frac{\mathrm{tr}\left(\boldsymbol{\varepsilon}\right)}{3} - \alpha_0\Delta\theta - \frac{\Omega_0}{3}\Delta c\right)\boldsymbol{I} + 2G_0\boldsymbol{\varepsilon}'. \tag{34}$$

The hydrostatic pressure follows with

$$p = -\frac{\mathrm{tr}\left(\boldsymbol{\sigma}\right)}{3} = -K_0\left(\mathrm{tr}\left(\boldsymbol{\varepsilon}\right) - 3\alpha_0\Delta\theta - \Omega_0\Delta c\right). \tag{35}$$

The second relation in Eq. (11) leads to the following entropy

$$\eta = \frac{3\alpha_0}{\rho}\left(3K_0\alpha_0\Delta\theta - p\right) + c_{\varepsilon,0}\ln\left(\frac{\theta}{\theta_0}\right) - \frac{Rc_\mathrm{max}}{\rho}\Big(c_\mathrm{n}\ln\left(c_\mathrm{n}\right) + \left(1 - c_\mathrm{n}\right)\ln\left(1 - c_\mathrm{n}\right)\Big). \tag{36}$$

The chemical potential is obtained from the third relation reading

$$\mu = \widetilde{\mu} + R\theta\ln\left(\frac{c_\mathrm{n}}{1 - c_\mathrm{n}}\right) + \Omega_0 p. \tag{37}$$

Thus, the chemical potential consists of a constant reference potential, a mixture entropic contribution and a pressure contribution. The mixture entropic contribution is monotonic in the concentration such that for concentrations close to zero, the contribution becomes negative infinity and for concentrations close to the maximum concentration, the contribution becomes positive infinity. An applied pressure also increases the chemical potential.

2.4. Closed set of equations

After the list of output quantities in Eq. (9) are defined thermodynamically consistent by algebraic equations, field equations for the displacement, the chemical potential and the temperature can be derived. The chemical potential is chosen as solution variable because its gradient determines the flux of diffusing species. Further, the usage of concentration as solution variable would force to rewrite the gradient of the chemical potential according to Eq. (13) which contains a third

derivative of the displacement. Third order derivatives would introduce difficulties for further usage of the field equations within the finite element method. In Villani et al. (2014), a chemo-mechanical model is introduced which considers the concentration instead of the chemical potential as solution variable. Highlighting the discretization in the next section, a comparison between these two choices is pointed out. Additionally, the usage of the chemical potential allows simulating open systems as the flux of diffusing species can directly be prescribed. Prescribing a chemical potential represents the exposure to a chemical atmosphere (cf. Di Leo and Anand, 2013). A concentration can only be prescribed directly on surfaces, where the pressure is zero and isothermal conditions exist. Otherwise, the concentration on a surface is a function of the chemical potential, the pressure and the temperature, cf. Eq. (37). Inserting Eq. (34) and the definition of strain into

$$\mathbf{0} = \operatorname{div}(\boldsymbol{\sigma}) + \rho \boldsymbol{b}, \tag{38}$$

a differential equation for the displacement field with dependencies on the concentration and the temperature is obtained. As proposed in Anand (2011) and further elaborated in Di Leo and Anand (2013) and Chester et al. (2015), the balance of diffusing species in Eq. (3) can be used to solve for the chemical potential. Since, the flux of diffusing species already contains the gradient of the chemical potential, the rate of concentration needs to be rewritten. So far, the chemical potential is a function $\mu = \hat{\mu}(\boldsymbol{\epsilon}, c, \theta)$, i.e. Eq. (37), which is now inverted into a function $c = \hat{c}(\boldsymbol{\epsilon}, \mu, \theta)$.The rate of the chemical potential can be derived generally by using $\hat{\mu}$ with

$$\dot{\mu} = \frac{\partial \hat{\mu}}{\partial \boldsymbol{\epsilon}} \cdot \dot{\boldsymbol{\epsilon}} + \frac{\partial \hat{\mu}}{\partial c}\dot{c} + \frac{\partial \hat{\mu}}{\partial \theta}\dot{\theta}. \tag{39}$$

The rate of concentration can be eliminated using Eq. (3) such that

$$\dot{\mu} = -\frac{\partial \hat{\mu}}{\partial c}\operatorname{div}(\boldsymbol{j}) + \frac{\partial \hat{\mu}}{\partial \boldsymbol{\epsilon}} \cdot \dot{\boldsymbol{\epsilon}} + \frac{\partial \hat{\mu}}{\partial \theta}\dot{\theta} \tag{40}$$

is obtained. The rate of concentration can be calculated explicitly with

$$\dot{c} = \frac{\partial \hat{c}}{\partial \mu}\dot{\mu} + \frac{\partial \hat{c}}{\partial \boldsymbol{\epsilon}} \cdot \dot{\boldsymbol{\epsilon}} + \frac{\partial \hat{c}}{\partial \theta}\dot{\theta} \tag{41}$$

and the following relations

$$\frac{\partial \hat{c}}{\partial \mu} = \left(\frac{\partial \hat{\mu}}{\partial c}\right)^{-1}, \qquad \frac{\partial \hat{c}}{\partial \boldsymbol{\epsilon}} = -\left(\frac{\partial \hat{\mu}}{\partial c}\right)^{-1}\frac{\partial \hat{\mu}}{\partial \boldsymbol{\epsilon}},$$
$$\frac{\partial \hat{c}}{\partial \theta} = -\left(\frac{\partial \hat{\mu}}{\partial c}\right)^{-1}\frac{\partial \hat{\mu}}{\partial \theta} \tag{42}$$

hold. For the present model, the function $\hat{c}$ is an implicit function. It needs to be mentioned that the chemical potential is not a preserved quantity such that the additional rates on the right-hand side embody a production of chemical potential. For the present model, Eq. (40) has the form

$$\dot{\mu} = -\left(\frac{R\theta}{c\left(1-c_{\mathrm{n}}\right)} + K_0\Omega_0^2\right)\operatorname{div}(\boldsymbol{j}) - K_0\Omega_0\operatorname{tr}(\dot{\boldsymbol{\epsilon}}) + \left(R\ln\left(\frac{c_{\mathrm{n}}}{1-c_{\mathrm{n}}}\right) + 3K_0\alpha_0\Omega_0\right)\dot{\theta}. \tag{43}$$

The equation of heat conduction in Eq. (14), which is solved for the temperature, obtains the following structure

$$\left(\rho c_{\varepsilon} + \theta\left(\frac{\partial \hat{c}}{\partial \theta}\right)^2\left(\frac{\partial \hat{c}}{\partial \mu}\right)^{-1}\right)\dot{\theta} = \left(\theta\frac{\partial \boldsymbol{\sigma}}{\partial \theta} - \theta\frac{\partial \hat{c}}{\partial \theta}\left(\frac{\partial \hat{c}}{\partial \mu}\right)^{-1}\frac{\partial \hat{c}}{\partial \boldsymbol{\epsilon}}\right) \cdot \dot{\boldsymbol{\epsilon}} - \theta\frac{\partial \hat{c}}{\partial \theta}\dot{\mu} + \rho w - \operatorname{div}(\boldsymbol{q}) - \boldsymbol{m} \cdot \boldsymbol{j}. \tag{44}$$

Taking the present model into account, the equation of heat conduction reads

$$\left(\rho c_{\varepsilon,0} + \theta\left(R\ln\left(\frac{c_{\mathrm{n}}}{1-c_{\mathrm{n}}}\right) + 3K_0\alpha_0\Omega_0\right)^2\left(\frac{R\theta}{c\left(1-c_{\mathrm{n}}\right)} + K_0\Omega_0^2\right)^{-1}\right)\dot{\theta} = \theta\left(-3K_0\alpha_0 + \left(R\ln\left(\frac{c_{\mathrm{n}}}{1-c_{\mathrm{n}}}\right) + 3K_0\alpha_0\Omega_0\right)\left(\frac{R\theta}{c\left(1-c_{\mathrm{n}}\right)} + K_0\Omega_0^2\right)^{-1}K_0\Omega_0\right)\operatorname{tr}(\dot{\boldsymbol{\epsilon}}) + \theta\left(R\ln\left(\frac{c_{\mathrm{n}}}{1-c_{\mathrm{n}}}\right) + 3K_0\alpha_0\Omega_0\right)\left(\frac{R\theta}{c\left(1-c_{\mathrm{n}}\right)} + K_0\Omega_0^2\right)^{-1}\dot{\mu} + \rho w - \operatorname{div}(\boldsymbol{q}) - \boldsymbol{m} \cdot \boldsymbol{j}. \tag{45}$$

Despite changes being made in the modeling of the specific free energy, the structure of the derived set of equations is equivalent to Anand (2011).

3. UEL implementation

3.1. Advantages of a user-defined element

Solving the set of the fully coupled nonlinear partial differential equations Eq. (38), Eq. (43) and (45) is nonstandard in commercial Finite Element (FE) solvers. Thus, the necessary steps as well as the needed residuals and tangents are highlighted to provide a self containing paper.

In the present case, the FE solver of ABAQUS is used as this solver allows to fully customize an element type. This ability is provided within the UEL subroutine which takes a discretized set of partial differential equations. Chester et al. (2015) provides the residuals and tangents for a chemo-mechanical model using a geometrically nonlinear theory. An equation of heat being uncoupled from the mechanics and the chemistry is provided in the appendix. This is extended and concretized for the present model. The input of the subroutine are updated values of each degree of freedom of each node of an element $\underline{d}_{\mathrm{E}}^{n+1} \in \mathbb{R}^{kN_{\mathrm{N}}}$ and a vector of the updated increments $\underline{\Delta d}_{\mathrm{E}}^{n+1} \in \mathbb{R}^{kN_{\mathrm{N}}}$ where k is the number of degrees of freedom (DOF) per node and N_{N} is the number of nodes per element. The output of the subroutine is the updated residual vector for all DOF of the element $\underline{R}_{\mathrm{E}}^{n+1} \in \mathbb{R}^{kN_{\mathrm{N}}}$ and the corresponding element stiffness matrix $\underline{\underline{K}}_{\mathrm{E}}^{n+1} \in \mathbb{R}^{(kN_{\mathrm{N}})\times(kN_{\mathrm{N}})}$ which describes how each nodal residual depends on each degree of freedom. These output quantities allow ABAQUS to set up the global Newton scheme

$$\underline{\underline{K}}^{n+1}\left(\underline{d}^{n+1}\right)\underline{\Delta d}^{n+1} = \underline{R}^{n+1}\left(\underline{d}^{n+1}\right), \quad \underline{d}^{n+1} = \underline{d}^{n} + \underline{\Delta d}^{n+1} \tag{46}$$

in standard manner with $\underline{d}^{n+1}, \underline{R}^{n+1}, \underline{\Delta d}^{n+1} \in \mathbb{R}^{kN}$ and $\underline{\underline{K}}^{n+1} \in \mathbb{R}^{(kN)\times(kN)}$ and a total number of nodes N. Solving general user-defined element formulations, ABAQUS uses its general nonlinear solver (cf. ABAQUS/Standard, 2020). A basic example for the general procedure of setting up an UEL for a scalar valued partial differential equation is provided in the Appendix A.

3.2. Discretization of the derived set of equations

The weak forms of Eqs. (38), (43) and (45) are obtained by multiplying each equation with a corresponding test function $\boldsymbol{w}_{\mathrm{u}}$, w_{μ} and w_{θ} and integrating over the whole body. The tensorial order of the test functions has to match the order of the corresponding field. These weak forms can now be discretized in time and space and the whole body is decomposed into several elements. In ABAQUS the integration over one element is needed.

Time discretization. The discretization in time for the solution variables reads

$$\operatorname{tr}(\dot{\boldsymbol{\epsilon}}) \approx \frac{\operatorname{tr}\left(\boldsymbol{\epsilon}^{n+1}\right) - \operatorname{tr}\left(\boldsymbol{\epsilon}^{n}\right)}{\Delta t^{n+1}}, \quad \dot{\mu} \approx \frac{\mu^{n+1} - \mu^{n}}{\Delta t^{n+1}}, \quad \dot{\theta} \approx \frac{\theta^{n+1} - \theta^{n}}{\Delta t^{n+1}}. \tag{47}$$

The material time derivatives are approximated by implicit Euler schemes and the convective contributions are neglected. The rate of concentration follows from Eq. (41).

Spatial discretization. Different shape functions are applicable for each degree of freedom, following

$$\begin{aligned} \boldsymbol{u} &\approx \underline{\underline{N}}_{\mathrm{u}}^{\mathsf{T}} \underline{d}_{\mathrm{E,u}}, \quad & w_{\mathrm{u}} &\approx \underline{\underline{N}}_{\mathrm{u}}^{\mathsf{T}} \underline{w}_{\mathrm{E,u}} \\ \mu &\approx \underline{N}_{\mu}^{\mathsf{T}} \underline{d}_{\mathrm{E},\mu}, \quad & w_{\mu} &\approx \underline{N}_{\mu}^{\mathsf{T}} \underline{w}_{\mathrm{E},\mu} \\ \theta &\approx \underline{N}_{\theta}^{\mathsf{T}} \underline{d}_{\mathrm{E},\theta}, \quad & w_{\theta} &\approx \underline{N}_{\theta}^{\mathsf{T}} \underline{w}_{\mathrm{E},\theta}. \end{aligned} \tag{48}$$

Choosing the different orders of shape functions is suitable as the stress given in Eq. (34) depends on the gradient of the displacement but directly on the temperature and to some extent on the chemical potential. Using linear shape functions for the temperature and the chemical potential implies quadratic shape functions for the displacement. The shape functions of the displacement are structured in the following way (cf. Fish and Belytschko, 2007)

$$\underline{\underline{N}}_{\mathrm{u}} = \begin{bmatrix} N_{\mathrm{u},1} & 0 & 0 \\ 0 & N_{\mathrm{u},1} & 0 \\ 0 & 0 & N_{\mathrm{u},1} \\ N_{\mathrm{u},2} & 0 & 0 \\ \vdots & \vdots & \vdots \\ 0 & 0 & N_{\mathrm{u},20} \end{bmatrix} \tag{49}$$

with $\underline{\underline{N}}_{\mathrm{u}} \in \mathbb{R}^{60\times 3}$. The vectors of displacement DOF and corresponding test fields are defined as $\underline{d}_{\mathrm{E,u}} \in \mathbb{R}^{60}$ and $\underline{w}_{\mathrm{E,u}} \in \mathbb{R}^{60}$, respectively. The shape functions of the temperature and the chemical potential are $\underline{N}_{\mu}$ and $\underline{N}_{\theta} \in \mathbb{R}^{8}$. Details on the shape functions are given in the Appendix B. The vectors containing the nodal DOF of the temperature and the chemical potential are $\underline{d}_{\mathrm{E},\mu}$, $\underline{d}_{\mathrm{E},\theta}$ and the test fields are $\underline{w}_{\mathrm{E},\mu}$ and $\underline{w}_{\mathrm{E},\theta} \in \mathbb{R}^{8}$. The B-matrices of the chemical potential and of the temperature can be found in the Appendix A in Eq. (A.6). The B-matrix for the displacement consist of the symmetric part of the displacement gradient with six independent components using the matrix–vector notation with ABAQUS convention such that

$$\underline{\underline{B}}_{\mathrm{u}} = \begin{bmatrix} \frac{\partial N_{\mathrm{u},1}}{\partial X_1} & 0 & 0 & \frac{\partial N_{\mathrm{u},1}}{\partial X_2} & \frac{\partial N_{\mathrm{u},1}}{\partial X_3} & 0 \\ 0 & \frac{\partial N_{\mathrm{u},1}}{\partial X_2} & 0 & \frac{\partial N_{\mathrm{u},1}}{\partial X_1} & 0 & \frac{\partial N_{\mathrm{u},1}}{\partial X_3} \\ 0 & 0 & \frac{\partial N_{\mathrm{u},1}}{\partial X_3} & 0 & \frac{\partial N_{\mathrm{u},1}}{\partial X_1} & \frac{\partial N_{\mathrm{u},1}}{\partial X_2} \\ \frac{\partial N_{\mathrm{u},2}}{\partial X_1} & 0 & 0 & \frac{\partial N_{\mathrm{u},2}}{\partial X_2} & \frac{\partial N_{\mathrm{u},2}}{\partial X_3} & 0 \\ \vdots & \vdots & \vdots & \vdots & \vdots & \vdots \\ 0 & 0 & \frac{\partial N_{\mathrm{u},20}}{\partial X_3} & 0 & \frac{\partial N_{\mathrm{u},20}}{\partial X_1} & \frac{\partial N_{\mathrm{u},20}}{\partial X_2} \end{bmatrix} \in \mathbb{R}^{60\times 6} \tag{50}$$

follows. The B-matrix is calculated using the gradient with respect to the reference configuration. This choice is due to more accurate results of strain distributions at the limit of the small deformation theory. It needs to be mentioned that the ABAQUS convention is a non-normalized notation which suffers disadvantages within vector calculations. Different conventions like Mandel notation and several others (cf. Helnwein, 2001) target these issues.

Element residuals. Inserting the discretized test functions into the weak forms of Eqs. (38), (43) and (45) leads to the following residuals. The residual vector for the displacement is

$$\underline{R}_{\mathrm{E,u}} = \int_{\partial \mathrm{V_E}} \underline{\underline{N}}_{\mathrm{u}} \underline{\bar{t}} \, \mathrm{d}a - \int_{\mathrm{V_E}} \underline{\underline{B}}_{\mathrm{u}} \underline{\sigma} \, \mathrm{d}v \tag{51}$$

where $\underline{\bar{t}} \mathrel{\hat{=}} \boldsymbol{\sigma}\boldsymbol{n}$ represents the traction vector on the boundary of the element volume V_E. The vector $\underline{\sigma}$ contains the six independent stress components in the same notation as chosen before in Eq. (50). For convenience, we adjust the notation of vectors and tensors according to their use. Body force densities are neglected. Using the general formulation, the residual vector for the chemical potential is

$$\begin{aligned} \underline{R}_{\mathrm{E},\mu} = &- \int_{\partial \mathrm{V_E}} \underline{N}_{\mu} \bar{j} \, \mathrm{d}a - \int_{\mathrm{V_E}} \underline{N}_{\mu} \frac{\partial \hat{c}}{\partial \mu} \dot{\mu} \, \mathrm{d}v + \int_{\mathrm{V_E}} \underline{\underline{B}}_{\mu} \underline{j} \, \mathrm{d}v \\ &- \int_{\mathrm{V_E}} \underline{N}_{\mu} \frac{\partial \hat{c}}{\partial \boldsymbol{\varepsilon}} \cdot \dot{\boldsymbol{\varepsilon}} \, \mathrm{d}v - \int_{\mathrm{V_E}} \underline{N}_{\mu} \frac{\partial \hat{c}}{\partial \theta} \dot{\theta} \, \mathrm{d}v \end{aligned} \tag{52}$$

where $\bar{j} \mathrel{\hat{=}} \boldsymbol{j} \cdot \boldsymbol{n}$ represents fluxes of diffusing species crossing the element boundary. In comparison to Villani et al. (2014), the rate of concentration is reformulated using the chemical potential instead of substituting the gradient of the chemical potential according to Eq. (13). The residual vector of the temperature is generally given by

$$\begin{aligned} \underline{R}_{\mathrm{E},\theta} = &- \int_{\partial \mathrm{V_E}} \underline{N}_{\theta} \bar{q} \, \mathrm{d}a - \int_{\mathrm{V_E}} \underline{N}_{\theta} \rho c_{\varepsilon} \dot{\theta} \, \mathrm{d}v \\ &+ \int_{\mathrm{V_E}} \underline{N}_{\theta} \theta \frac{\partial \hat{\boldsymbol{\sigma}}}{\partial \theta} \cdot \dot{\boldsymbol{\varepsilon}} \, \mathrm{d}v \\ &+ \int_{\mathrm{V_E}} \underline{N}_{\theta} \theta \frac{\partial \hat{\mu}}{\partial \theta} \dot{c} \, \mathrm{d}v - \int_{\mathrm{V_E}} \underline{N}_{\theta} \boldsymbol{m} \cdot \boldsymbol{j} \, \mathrm{d}v + \int_{\mathrm{V_E}} \underline{\underline{B}}_{\theta} \underline{q} \, \mathrm{d}v \end{aligned} \tag{53}$$

where $\bar{q} \mathrel{\hat{=}} \boldsymbol{q} \cdot \boldsymbol{n}$ corresponds to heat fluxes on the element boundary and $\underline{q}$ represents the vector notation of the internal heat flux. The concretized derivates are given in the Appendix C.

Element stiffness matrix. The element stiffness matrix obtains the following structure

$$\underline{\underline{K}}_{\mathrm{E}} = \begin{bmatrix} \underline{\underline{K}}_{\mathrm{E,uu}} & \underline{\underline{K}}_{\mathrm{E,u}\mu} & \underline{\underline{K}}_{\mathrm{E,u}\theta} \\ \underline{\underline{K}}_{\mathrm{E},\mu\mathrm{u}} & \underline{\underline{K}}_{\mathrm{E},\mu\mu} & \underline{\underline{K}}_{\mathrm{E},\mu\theta} \\ \underline{\underline{K}}_{\mathrm{E},\theta\mathrm{u}} & \underline{\underline{K}}_{\mathrm{E},\theta\mu} & \underline{\underline{K}}_{\mathrm{E},\theta\theta} \end{bmatrix}. \tag{54}$$

Each row is connected to one residual vector and each column contains the derivates by on degree of freedom. Taking the displacement as one degree of freedom, the first row contains the entries $\underline{\underline{K}}_{\mathrm{E,uu}} \in \mathbb{R}^{60\times 60}$, $\underline{\underline{K}}_{\mathrm{E,u}\mu} \in \mathbb{R}^{60\times 8}$ and $\underline{\underline{K}}_{\mathrm{E,u}\theta} \in \mathbb{R}^{60\times 8}$ which represent the derivatives of the displacement residual in Eq. (51). Due to the choice of solving for the chemical potential, the derivative

$$\underline{\underline{K}}_{\mathrm{E,uu}} = -\frac{\partial \underline{R}_{\mathrm{E,u}}}{\partial \underline{d}_{\mathrm{E,u}}} = \int_{\mathrm{V_E}} \underline{\underline{B}}_{\mathrm{u}} \frac{\partial \hat{\underline{\sigma}}}{\partial \underline{\varepsilon}} \underline{\underline{B}}_{\mathrm{u}}^{\mathsf{T}} \, \mathrm{d}v - \int_{\mathrm{V_E}} \underline{\underline{B}}_{\mathrm{u}} \frac{\partial \hat{\underline{\sigma}}}{\partial c} \left(\frac{\partial \hat{c}}{\partial \underline{\varepsilon}} \right)^{\mathsf{T}} \underline{\underline{B}}_{\mathrm{u}}^{\mathsf{T}} \, \mathrm{d}v \tag{55}$$

contains a second term as the concentration itself depends on the strain field while the stress is a function $\boldsymbol{\sigma} = \hat{\boldsymbol{\sigma}}(\boldsymbol{\varepsilon}, c, \theta)$. The derivative with respect to the chemical potential

$$\underline{\underline{K}}_{\mathrm{E,u}\mu} = -\frac{\partial \underline{R}_{\mathrm{E,u}}}{\partial \underline{d}_{\mathrm{E},\mu}} = \int_{\mathrm{V_E}} \underline{\underline{B}}_{\mathrm{u}} \frac{\partial \hat{\underline{\sigma}}}{\partial c} \frac{\partial \hat{c}}{\partial \mu} \underline{N}_{\mu}^{\mathsf{T}} \, \mathrm{d}v \tag{56}$$

consists of a single term, similar to Villani et al. (2014). The derivative with respect to the temperature

$$\underline{\underline{K}}_{\mathrm{E,u}\theta} = -\frac{\partial \underline{R}_{\mathrm{E,u}}}{\partial \underline{d}_{\mathrm{E},\theta}} = \int_{\mathrm{V_E}} \underline{\underline{B}}_{\mathrm{u}} \frac{\partial \hat{\underline{\sigma}}}{\partial \theta} \underline{N}_{\theta}^{\mathsf{T}} \, \mathrm{d}v - \int_{\mathrm{V_E}} \underline{\underline{B}}_{\mathrm{u}} \frac{\partial \hat{\underline{\sigma}}}{\partial c} \frac{\partial \hat{c}}{\partial \theta} \underline{N}_{\theta}^{\mathsf{T}} \, \mathrm{d}v \tag{57}$$

contains two terms. One due to the explicit dependency of the stress on the temperature and one due to the implicit dependency caused by the concentration. For the residual in Eq. (52), the tangents generally read

$$\begin{aligned} \underline{\underline{K}}_{\mathrm{E},\mu\mathrm{u}} &= -\frac{\partial \underline{R}_{\mathrm{E},\mu}}{\partial \underline{d}_{\mathrm{E,u}}} \\ &= \int_{\mathrm{V_E}} \underline{N}_{\mu} \left(\frac{\partial \hat{c}}{\partial \underline{\varepsilon}} \right)^{\mathsf{T}} \underline{\underline{B}}_{\mathrm{u}}^{\mathsf{T}} \, \mathrm{d}v + \int_{\mathrm{V_E}} \underline{\underline{B}}_{\mu} \frac{\partial \hat{\underline{j}}}{\partial c} \left(\frac{\partial \hat{c}}{\partial \underline{\varepsilon}} \right)^{\mathsf{T}} \underline{\underline{B}}_{\mathrm{u}}^{\mathsf{T}} \, \mathrm{d}v, \end{aligned} \tag{58}$$

$$\begin{aligned} \underline{\underline{K}}_{\mathrm{E},\mu\mu} = -\frac{\partial \underline{R}_{\mathrm{E},\mu}}{\partial \underline{d}_{\mathrm{E},\mu}} &= \int_{\mathrm{V_E}} \underline{N}_{\mu} \frac{\partial \hat{c}}{\partial \mu} \underline{N}_{\mu}^{\mathsf{T}} \, \mathrm{d}v \\ &+ \int_{\mathrm{V_E}} \underline{\underline{B}}_{\mu} \left(\frac{\partial \hat{\underline{j}}}{\partial c} \frac{\partial \hat{c}}{\partial \mu} \underline{N}_{\mu}^{\mathsf{T}} + \frac{\partial \hat{\underline{j}}}{\partial \underline{m}} \underline{\underline{B}}_{\mu}^{\mathsf{T}} \right) \mathrm{d}v \end{aligned} \tag{59}$$

and

$$\begin{aligned} \underline{\underline{K}}_{\mathrm{E},\mu\theta} = -\frac{\partial \underline{R}_{\mathrm{E},\mu}}{\partial \underline{d}_{\mathrm{E},\theta}} &= \int_{\mathrm{V_E}} \underline{N}_{\mu} \frac{\partial \hat{c}}{\partial \theta} \underline{N}_{\theta}^{\mathsf{T}} \, \mathrm{d}v \\ &+ \int_{\mathrm{V_E}} \underline{\underline{B}}_{\mu} \left(\frac{\partial \hat{\underline{j}}}{\partial c} \frac{\partial \hat{c}}{\partial \theta} + \frac{\partial \hat{\underline{j}}}{\partial \theta} \right) \underline{N}_{\theta}^{\mathsf{T}} \, \mathrm{d}v \end{aligned} \tag{60}$$

with $\boldsymbol{j} = \hat{\boldsymbol{j}}(c, \theta, \boldsymbol{m})$. In contrast to Villani et al. (2014), each tangent has a dependency on the rate of concentration, but the tangent in Eq. (59) does not depend on higher order derivatives of the shape

functions. The partial derivatives of the concentration and its rate are given in detail in the Appendix C. Motivated by Villani et al. (2014) and Barrera et al. (2016), a perforated plate loaded in one direction is used to compare numerical results with analytical results of the chemo-mechanical coupling. Results of that can be found in the Appendix D. The thermal tangents read

$$\begin{aligned}\underline{\underline{K}}_{\mathrm{E},\theta\mathrm{u}} = -\frac{\partial \underline{R}_{\mathrm{E},\theta}}{\partial \underline{d}_{\mathrm{E,u}}} &= -\int_{\mathrm{V_E}} \underline{N}_\theta \theta \frac{\partial \hat{\boldsymbol{\sigma}}}{\partial \theta} \cdot \boldsymbol{I} \frac{1}{\Delta t} \underline{\underline{B}}_{\mathrm{u}}^{\mathrm{T}} \,\mathrm{d}v \\ &- \int_{\mathrm{V_E}} \underline{N}_\theta \theta \left(\frac{\partial^2 \hat{\mu}}{\partial \theta \partial c} \dot{c} \left(\frac{\partial \hat{c}}{\partial \underline{\varepsilon}} \right)^{\mathrm{T}} + \frac{\partial \hat{\mu}}{\partial \theta} \left(\frac{\partial \hat{c}}{\partial \underline{\varepsilon}} \right)^{\mathrm{T}} \right) \underline{\underline{B}}_{\mathrm{u}}^{\mathrm{T}} \,\mathrm{d}v \\ &+ \int_{\mathrm{V_E}} \underline{N}_\theta \boldsymbol{m} \cdot \frac{\partial \hat{\underline{j}}}{\partial c} \left(\frac{\partial \hat{c}}{\partial \underline{\varepsilon}} \right)^{\mathrm{T}} \underline{\underline{B}}_{\mathrm{u}}^{\mathrm{T}} \,\mathrm{d}v, \end{aligned} \tag{61}$$

$$\begin{aligned}\underline{\underline{K}}_{\mathrm{E},\theta\mu} = -\frac{\partial \underline{R}_{\mathrm{E},\theta}}{\partial \underline{d}_{\mathrm{E,u}}} &= -\int_{\mathrm{V_E}} \underline{N}_\theta \theta \left(\frac{\partial^2 \hat{\mu}}{\partial \theta \partial c} \dot{c} \frac{\partial \hat{c}}{\partial \mu} + \frac{\partial \hat{\mu}}{\partial \theta} \frac{\partial \hat{c}}{\partial \mu} \right) \underline{N}_\mu^{\mathrm{T}} \,\mathrm{d}v \\ &+ \int_{\mathrm{V_E}} \underline{N}_\theta \left(\underline{j}^{\mathrm{T}} \underline{\underline{B}}_\mu^{\mathrm{T}} + \underline{m}^{\mathrm{T}} \frac{\partial \hat{\underline{j}}}{\partial \underline{m}} \underline{\underline{B}}_\mu^{\mathrm{T}} + \boldsymbol{m} \cdot \frac{\partial \hat{\underline{j}}}{\partial c} \frac{\partial \hat{c}}{\partial \mu} \frac{\partial m}{\partial c} \underline{N}_\mu^{\mathrm{T}} \right) \mathrm{d}v \end{aligned} \tag{62}$$

and

$$\begin{aligned}\underline{\underline{K}}_{\mathrm{E},\theta\theta} = -\frac{\partial \underline{R}_{\mathrm{E},\theta}}{\partial \underline{d}_{\mathrm{E},\theta}} &= \int_{\mathrm{V_E}} \underline{N}_\theta \frac{\rho c_\varepsilon}{\Delta t} \underline{N}_\theta^{\mathrm{T}} \,\mathrm{d}v - \int_{\mathrm{V_E}} \underline{N}_\theta \frac{\partial \hat{\boldsymbol{\sigma}}}{\partial \theta} \cdot \dot{\boldsymbol{\varepsilon}} \underline{N}_\theta^{\mathrm{T}} \,\mathrm{d}v \\ &- \int_{\mathrm{V_E}} \underline{N}_\theta \left(\frac{\partial \hat{\mu}}{\partial \theta} \dot{c} + \theta \frac{\partial^2 \hat{\mu}}{\partial \theta \partial c} \frac{\partial \hat{c}}{\partial \theta} + \theta \frac{\partial \hat{\mu}}{\partial \theta} \frac{\partial \hat{c}}{\partial \theta} \right) \underline{N}_\theta^{\mathrm{T}} \,\mathrm{d}v \\ &+ \int_{\mathrm{V_E}} \underline{N}_\theta \left(\boldsymbol{m} \cdot \frac{\partial \hat{\underline{j}}}{\partial \theta} + \boldsymbol{m} \cdot \frac{\partial \hat{\underline{j}}}{\partial c} \frac{\partial \hat{c}}{\partial \theta} \right) \underline{N}_\theta^{\mathrm{T}} \,\mathrm{d}v - \int_{\mathrm{V_E}} \underline{\underline{B}}_\theta \frac{\partial \hat{\underline{q}}}{\partial \underline{g}} \underline{\underline{B}}_\theta^{\mathrm{T}} \,\mathrm{d}v. \end{aligned} \tag{63}$$

Due to the consideration of linear elasticity, the derivate $\partial\hat{\boldsymbol{\sigma}}/\partial\theta$ is constant. The derivative $\partial\hat{\mu}/\partial\theta$ depends on the concentration. Analytical expression for all derivates in Eqs. (61), (62) and (63) can be found in the Appendix C.

Remarks on the UEL subroutine. One single vector of nodal DOF is provided within the UEL subroutine. The standard ordering of the DOF is per node such that the DOF of the first node are given first, then the ones of the second node and so on. Thus, it is useful to reorder the DOF either in the beginning of the subroutine or to change the standard ordering within the *.inp*-file. More details about the defining the order of DOF are available in ABAQUS/Standard (2020). After the reordering of the nodel DOF, the subroutine is basically separated into two loops for both integration procedures on the volume and the surface. The volume integrals use reduced integration such that the material behavior is needed on eight integration points only.

Settings in the ABAQUS .inp-file. The element definition within the *.inp*-file uses the nodal DOF *1, 2, 3, 11, 12*. To activate the temperature DOF *11, 12, ...*, a thermal material has to be defined additionally. The usage of the thermal DOF enables the *Coupled-Temperature-Displacement* analysis which contains the automatic time incrementation. The time increment is controlled by a maximum allowable change of chemical potential or temperature which is set to $\max(\Delta\mu, \Delta\theta) = 10\,\mathrm{J/mol}$. This restriction is needed to ensure accurate time integration otherwise a loss of mass can appear depending on the chosen material parameters.

Visualization of user elements via ABAQUS/viewer. The visualization of user elements via ABAQUS/Viewer is not built-in supported as the morphology of the element is not accessible (cf. ABAQUS/Standard, 2020), thus, some workarounds are needed. In the following sections, two ways of dealing with this issue are used. The first one uses so-called dummy elements which have the same morphology as the user elements in terms of shape functions and number of integration points. The mesh of user elements is mirrored by a mesh of these dummy elements using the same nodes but a different element numbering. During the element routine, the variables of each integration point of a user element is mapped on the corresponding dummy element where a number of user variables is defined via the UVARM subroutine. The dummy mesh can be created in ABAQUS/CAE by copying a meshed part and changing the global numbering of the second part. More details can be found in Chester et al. (2015). The second way involves the ABAQUSER tool developed by Roth et al. (2012). Instead of processing the dummy elements during the simulation, the mapping of the user element state variables (SDV) is done in a post-processing step. The output of a simulation is saved in a results file which is used to produce an output database involving an *.info*-file containing missing information about the element morphology.

4. Numerical study

4.1. General procedure

Based on the validation illustrated in Barrera et al. (2016), an investigation on the involved couplings is developed. In Anand (2011) and Mianroodi et al. (2022), the investigation of the precise nature of coupling effects is named as an ongoing field of research which should gain some interest. With the following work, one possible way of doing so is provided. The steadily increasing complexity in terms of coupled behavior is combined with the simplicity of a 1D geometry. For the presented model consisting of three fields, three one-field submodels, three two-field submodels and the overall three-field model can be defined. The one-field and two-field submodels are derived by excluding one or two fields, respectively. Table 1 lists an overview of the considered models.

Table 1
Submodels of the presented model.

Identifier	Model type	Included fields
$\mathrm{M_M}$	one-field – mechanical	$\boldsymbol{u}$
$\mathrm{M_C}$	one-field – chemical	μ
$\mathrm{M_T}$	one-field – thermal	θ
$\mathrm{M_{CM}}$	two-field – chemo-mechanical	$\boldsymbol{u}$, μ
$\mathrm{M_{TM}}$	two-field – thermo-mechanical	$\boldsymbol{u}$, θ
$\mathrm{M_{TC}}$	two-field – thermo-chemical	μ, θ
$\mathrm{M_{TCM}}$	three-field – thermo-chemo-mechanical	$\boldsymbol{u}$, μ, θ

The goal is to accomplish a methodical procedure to understand quantitatively the physical couplings of the multi-field model. The basic hypothesis is that each field has its own behavior such that multiple fields can be superposed. Though, each coupling term can lead to changes of the overall result compared to the superposed result only. The focus is shifted on the actual model behavior by using a one-dimensional geometry and a set of boundary conditions, e.g. Dirichlet conditions and zero flux conditions. This choice is in contrast to Barrera et al. (2016) as the chemo-mechanical coupling is validated neglecting the dependency of the concentration on the stress.

The same set of boundary conditions is used for each submodel, but only the boundary conditions for the fields active are considered. The deactivated fields do not change during the simulations. For example if a temperature is prescribed at a bound, the boundary condition works for the models $\mathrm{M_T}$, $\mathrm{M_{TM}}$, $\mathrm{M_{TC}}$ and $\mathrm{M_{TCM}}$ only. The single field behavior $\mathrm{M_T}$ takes the role of a reference behavior. The analytic solutions for the uncoupled equation of heat conduction and the uncoupled equation of diffusion are identical. In Barrera et al. (2016), an expression for the analytic solution in case of 1D is given.

The following investigation provides a hint whether specific physical couplings have a significant influence or not. For example if a thermal boundary condition is prescribed, different results for $\mathrm{M_{TM}}$ and $\mathrm{M_{TC}}$ are obtained. Comparing these two results to the result obtained for $\mathrm{M_{TCM}}$ leads either to the conclusion that the chemo-mechanical coupling is weak, if the $\mathrm{M_{TCM}}$ result is just a superposition, or, if the results have significant differences, the conclusion would be a strong coupling. This conclusion does depend on the choice of material parameters as

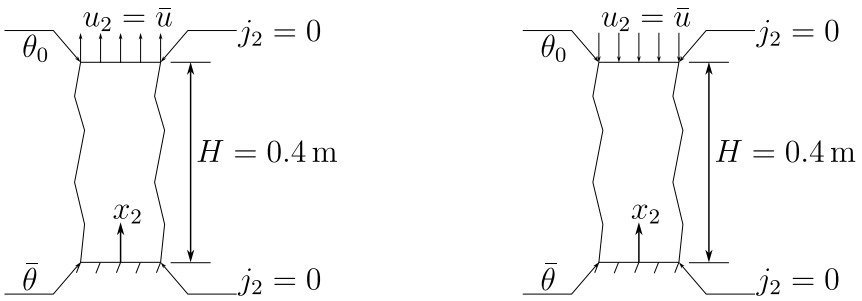

(a) Strip section in a closed system under tension

(b) Strip section in a closed system under compression

Fig. 1. Boundary conditions of a strip section with height $H = 0.4\,\mathrm{m}$.

Table 2
Material parameters used in the closed and open system simulations.

Parameter	Value
E_0	200.0 GPa
ν_0	0.3
$\tilde{\mu}$	0.0 J mol^{-1}
R	8.3145 J mol^{-1} K^{-1}
Ω_0	$1.0 \cdot 10^{-5}$ m^3 mol^{-1}
$c_{\max}$	$1.0 \cdot 10^{5}$ mol m^{-3}
D_0	$1.0 \cdot 10^{-8}$ m^2 s^{-1}
κ_0	$1.0 \cdot 10^{2}$ W m^{-1} K^{-1}
α_0	$1.0 \cdot 10^{-5}$ K^{-1}
ρ	$8.0 \cdot 10^{3}$ kg m^{-3}
$c_{\varepsilon,0}$	$5.0 \cdot 10^{2}$ J kg^{-1} K^{-1}

well. If the molar volume is negligible, a chemo-mechanical coupling would not be present.

The material parameters used for all cases are listed in Table 2. These parameters are motivated by the combination of steel and hydrogen. The chemo-mechanical parameters are adapted from Di Leo and Anand (2013).

Note that the following results do not contain completely general conclusions as they do depend on the choice of the material parameters above.

4.2. Closed system

A strip of infinite length is considered such that gradients in x_1 and x_3 vanish. The mechanical displacement u_1 and u_3 are constrained. In Fig. 1 the strip with its different sets of boundary conditions is depicted. The height of the strip is $H = 0.4\,\mathrm{m}$. A mesh consisting of 8000 elements with a size of $l_{\mathrm{el}} = 1.0 \cdot 10^{-4}\,\mathrm{m}$ arranged in two columns is created.

Simulation setup. Both sets of boundary conditions in Fig. 1 represent closed systems as the flux of diffusing species is set to zero on both ends. The difference between Fig. 1(a) and Fig. 1(b) is the sign of the applied displacement on the top end. The boundary conditions for the displacement field are $u_2(0) = 0.0\,\mathrm{m}$, $u_2(H) = \bar{u}$ and $u_2(H) = -\bar{u}$ with $\bar{u} = 0.002\,\mathrm{m}$, respectively. The boundary conditions of the temperature field are $\theta(0) = \bar{\theta}$ and $\theta(H) = \theta_0$ with $\bar{\theta} = 1000.0\,\mathrm{K}$. The total simulation time is divided into two steps with a first step ramping up linearly the prescribed values and a second step intended to let the system relax into an equilibrium state. The periods of time are $t_{\mathrm{Step1}} = 100.0\,\mathrm{s}$ for the ramping step and $t_{\mathrm{Step2}} = 8.5 \cdot 10^{6}\,\mathrm{s}$ for the diffusion step. The initial conditions are $\mu_0 = -9707.562\,\mathrm{J/mol}$ for the chemical potential referring to an initial species concentration of $c_0 = 2000.0\,\mathrm{mol/m^3}$ at a temperature of $\theta_0 = 300.0\,\mathrm{K}$.

Results after the loading step. The results at the end of the loading step are depicted first in Fig. 2, Fig. 3 and Fig. 4. Strain, temperature, pressure, chemical potential, species concentration and flux of diffusing species are considered of interest as they are either prescribed at the bounds or depend on all active fields.

There are two types of strain distributions in Fig. 2(a) for each loading case. The first one occurs in the submodels $\mathrm{M_M}$ and $\mathrm{M_{CM}}$ independent of the temperature. The second one focusing on the lower boundary is referred to the prescribed temperature. While the first one is homogeneous and based on the prescribed displacement depending on the loading case, the second one has a larger magnitude near the lower boundary due to the thermal coupling. Thus, to satisfy the prescribed displacement on the upper boundary, a lower magnitude in the colder regions is obtained. The different loading cases lead to vertical shifts only. The thermo-chemical coupling does not lead to significant changes.

In Fig. 2(b), slight variations in temperature depending on the active fields occur, though, the overall temperature distributions are identical and independent on the loading case and the model. All distributions are pretty much identical to the reference submodel $\mathrm{M_T}$. This result is strongly affected by the heat conductivity as its magnitude defines the speed at which the heat flows. If the heat conductivity is low enough, local changes in temperature due to chemical heat production cannot be balanced out immediately.

The pressure in Fig. 3(a) corresponds to strain in Fig. 2(a) receiving the same vertical shift depending on the loading case. A pressure gradient due to the increased temperature at the lower boundary occurs. The chemical potentials depicted in Fig. 3(b) do change significantly depending on the pressure as well as the temperature. The prescribed temperature decreases the chemical potential the most by a factor of three in the $\mathrm{M_{TC}}$ model. The different load cases lead to vertical shifts again while the compressive loading in the $\mathrm{M_{TCM}}$ model leads to the highest chemical potential. The gradient of the chemical potential near the lower boundary is reduced in the $\mathrm{M_{TCM}}$ model by the pressure, though, the dependency by the pressure does not fully counter the influence of the temperature.

Nevertheless, the chemical potential does have strong coupling dependencies of the pressure and the temperature.

Depending on the gradient of the chemical potential seen in Fig. 3(b) fluxes of diffusing species depicted in Fig. 4(a) occur. The fluxes are zero at both ends, though a motion of diffusing species directed to the lower boundary is received. The magnitude of the flux is reduced in the $\mathrm{M_{CM}}$ model due to the influence of the pressure on chemical potential. The diffusion is mainly induced by the applied

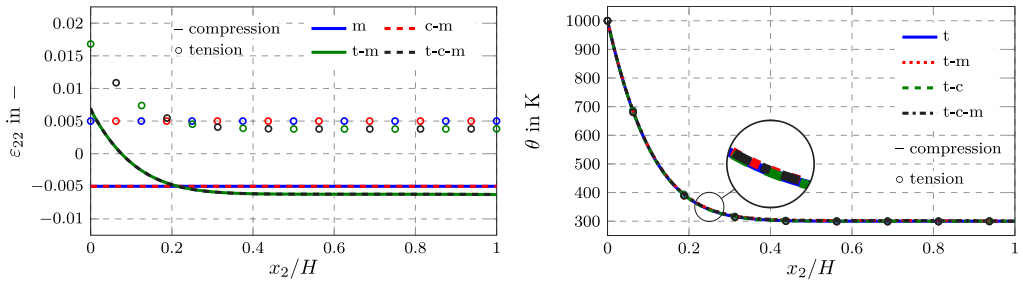

(a) Comparison of longitudinal strains resulting from different models

(b) Comparison of temperatures resulting from different models

Fig. 2. Strain and temperature in a closed system with a prescribed elongation at $t = t_{\text{Step1}}$.

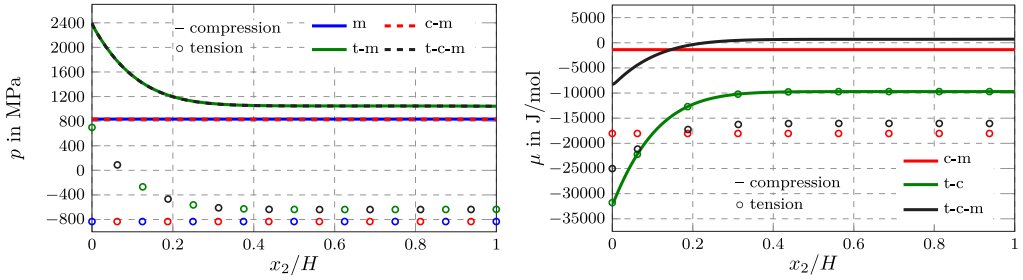

(a) Comparison of pressures resulting from different models

(b) Comparison of chemical potentials resulting from different models

Fig. 3. Pressure and chemical potential in a closed system with a prescribed elongation at $t = t_{\text{Step1}}$.

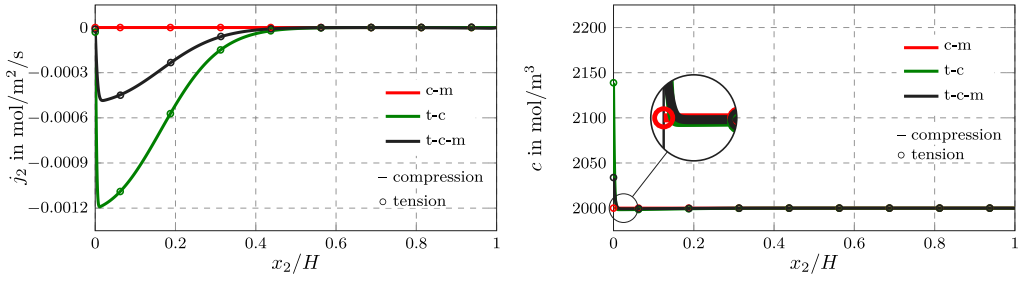

(a) Comparison of fluxes of diffusing species resulting from different models

(b) Comparison of concentrations in different models

Fig. 4. Flux of diffusing species and concentration resulting from a closed system with a prescribed elongation at $t = t_{\text{Step1}}$.

temperature, so this is the thermodiffusive phenomenon, but the active mechanical field does influence this phenomenon. Although, cross-coupling effects are not included within the fluxes, the temperature does indirectly lead to a gradient of the chemical potential which then leads to a motion of diffusing species. As the flux of diffusing species depends on the gradient of the chemical potential only, the mechanical loading case does not have any influence here. In Fig. 4(b), the concentrations according to the fluxes are depicted. Right at the lower end, an increase of concentration is seen while a slight decrease further upwards the strip occurs. The change in concentration is basically driven by the prescribed temperature at the lower boundary and the thermodiffusion.

The prescribed displacement boundary conditions lead to volume changes of about ±0.5%, cf. Fig. 2(a), which does not affect the concentration, cf. Fig. 4(b). With a constant concentration in a slightly larger volume, the amount of species has artificially increased. In the context of a geometrically linear theory, this shortcoming has to be accepted, though the error is proportional to the volume change. If larger volume changes have to be considered, the results of the presented theory should be interpreted with caution.

Results after the diffusion step. At the end of this second step, thermodynamic equilibrium is achieved.

In comparison to the preceding result in Fig. 2(a), three types of strain distributions are obtained in Fig. 5(a), while the different loading cases lead to a vertical shift only. The submodels without temperature have no variation, but between the M_{TM} submodel and the M_{TCM} model occurs a different strain distribution. The maximum values for the fully coupled model are even higher right at the bounds. This result emphasizes the thermo-chemical coupling and the induced action on the strain. For all models, the temperatures Fig. 5(b) remain identical to the reference M_T submodel after the diffusion is finished.

The pressure in Fig. 6(a) corresponds to the strains in Fig. 5(a) such that the highest pressure is on the lower bound. In Fig. 6(b) a steady state is reached for every model as the chemical potential is homogeneous. In the M_{TC} model, the resulting chemical potential is the lowest. Considering the initial chemical potential at around

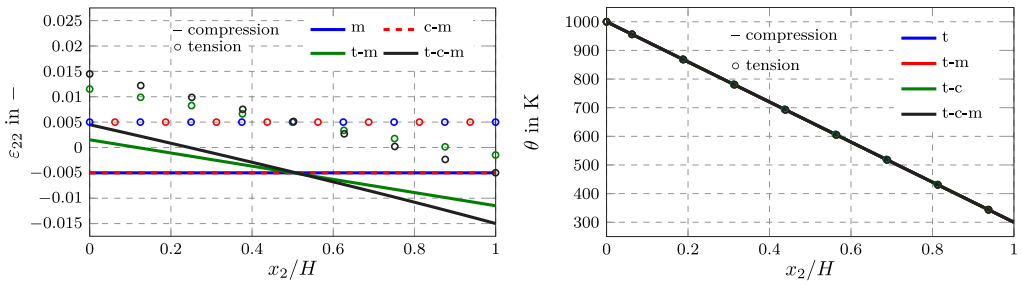

(a) Comparison of longitudinal strains resulting from different models

(b) Comparison of temperatures resulting from different models

Fig. 5. Strain and temperature in a closed system with a prescribed elongation at $t = t_{\text{Step2}}$.

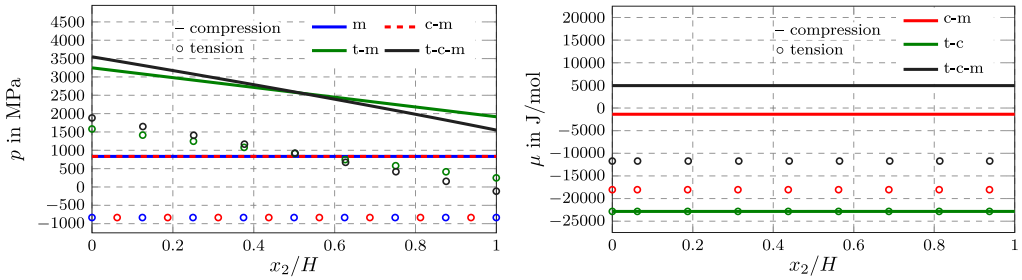

(a) Comparison of pressures resulting from different models

(b) Comparison of chemical potentials resulting from different models

Fig. 6. Pressure and chemical potential in a closed system with a prescribed elongation at $t = t_{\text{Step2}}$.

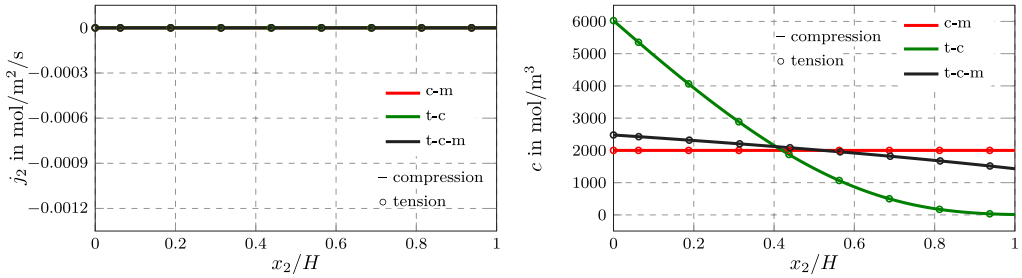

(a) Comparison of fluxes of diffusing species resulting from different models

(b) Comparison of concentrations resulting from different models

Fig. 7. Flux of diffusing species and concentration in a closed system with a prescribed elongation at $t = t_{\text{Step2}}$.

$-10000.0\,\text{J/mol}$, the compressive loading leads to a positive shift while the tensile loading shifts the chemical potential to the negative. The results of the M_{TCM} models are highly nonlinear as for both loading cases a positive shift is obtained. This is unexpected as the M_{TC} model has the lowest chemical potential. The explanation of this behavior is build-up on the positive shifting due to compressive pressures. The increased temperature induces high pressures leading to the overall positive shift of the chemical potential.

The fluxes of diffusing species in Fig. 7(a) are vanished in the equilibrium state. The concentrations in Fig. 7(b) differ for each model, but the results are independent of the loading case. The M_{CM} submodel preserves the initial concentration as the thermal diffusion is not active for this submodel. The temperature increase at the lower boundary induces thermal diffusion such that the concentration in the M_{TC} submodel is shifted significantly to the lower bound, while the upper boundary is dried out. The drastic influence of the thermal diffusion is reduced in the M_{TCM} model such that a shift to the lower boundary is still obtained, but the resulting concentrations right at the bounds do not vary that much as in the M_{TC} model.

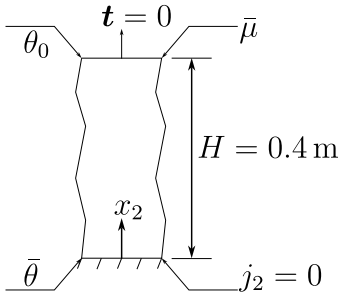

Fig. 8. Strip section in an open system.

The lessons learned in the presented cases are that the temperature has a large impact on the mechanical and the chemical behavior and that the level of the chemical potential is shifted through the prescribed mechanical state which can be relevant for the interaction of the solid

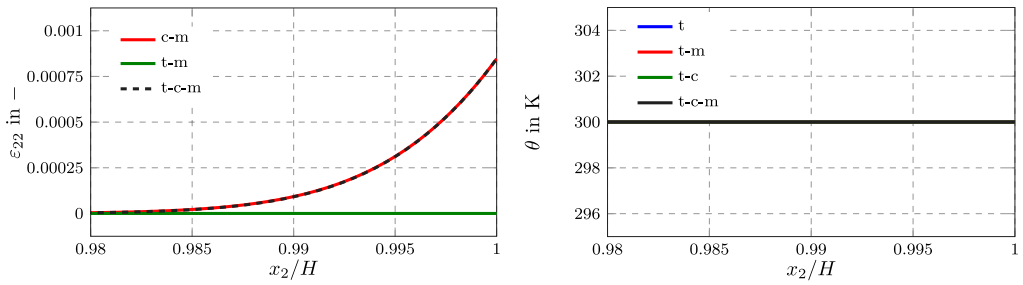

(a) Comparison of longitudinal strains resulting from different models

(b) Comparison of temperatures resulting from different models

Fig. 9. Strain and temperature in an open system at $t = t_{\text{Step1}}$.

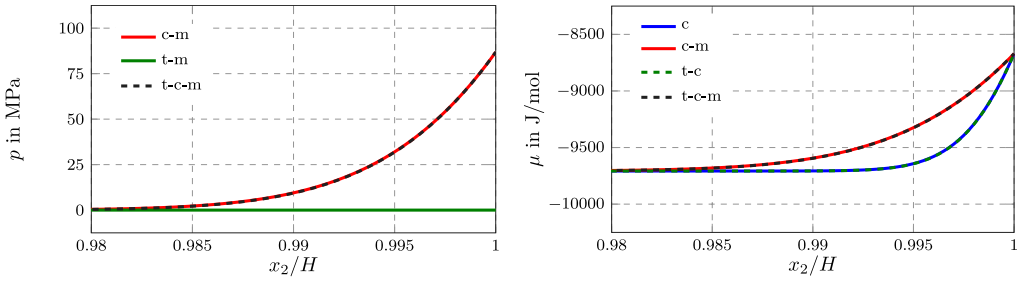

(a) Comparison of pressures resulting from different models

(b) Comparison of chemical potentials resulting from different models

Fig. 10. Pressure and chemical potential in an open system at $t = t_{\text{Step1}}$.

with the environment. For example if a specific chemical environment is provided the exchange of diffusing species can be controlled by elongation and compression of the part affecting the direction of the gradient of the chemical potential.

4.3. Open system

Simulation setup. The open system differs from the previous case in such a way that an exchange of diffusing species with the environment is allowed on the upper bound, cf. Fig. 8. To accomplish this behavior the chemical potential is prescribed by $\mu(x_2 = H) = \hat{\mu}$ with $\hat{\mu} = -8670.607\,\text{J/mol}$ referring to a concentration of $c = 3000.0\,\text{mol/m}^3$ and a temperature of $\theta = 300.0\,\text{K}$ at a zero pressure state. This chemical potential leads to a flux of diffusing species directed into the strip. The prescribed displacement is replaced with a zero traction vector. The prescribed temperature at the lower boundary and the initial conditions are propagated from the previous cases.

Results after the loading step. The following plots focus on the upper boundary at the end of the first step. On the lower bound, the results are identical to the preceding results due to the same prescribed temperature.

The strain in Fig. 9(a) increases near the upper boundary at least for the submodels having the chemical field active. The results of the M_{CM} submodel and the M_{TCM} model are identical, which is reasonable as the temperature depicted in Fig. 9(b) does not change at all near the upper bound.

The pressures in Fig. 10(a) are positive and follow straight from the strains in Fig. 9(a). The chemical potentials in Fig. 10(b) are different depending on the mechanical field active or not. The mechanical behavior leads to a less steep gradient of the chemical potential on the cost of greater spatial affection. While the gradient in the models M_C and M_{TC} is within 0.5–0.7% deep inside the strip, a depth of 1.3–1.5% is obtained in the M_{CM} and M_{TCM} models.

The fluxes of diffusing species in Fig. 11(a) vary accordingly to the chemical potentials. Through the different slops, the fluxes are different in terms of magnitude and depth as well. The fluxes of diffusing species without the mechanical field active are four times higher right at the bound, but they tend to zero within the first 0.5–0.7% of the solid. The fluxes of diffusing species with the mechanical field reach a depth of about 1.3–1.5%. Thus, the amount of diffusing species moved inside the solid has changed as well. In Fig. 11(b) the concentration of the models without the mechanical field active reaches the expected value of $3000.0\,\text{mol/m}^3$ while the concentration in the M_{CM} submodel and M_{TCM} model reaches less than 20% of the prescribed change right at the bound. Though, the change of concentration occurs deeper within the material. The actual values depend on the bulk modulus and the molar volume. If both parameters increase, the spatial distribution is suggested to reach deeper inside due to the higher pressure obtained. The actual amount of species moving inside the solid material would decrease due to the coupling of pressure and chemical potential.

A clear impact of the mechanical response on the diffusive behavior is obtained. The diffusing species entering the solid material leads to a pressure which counters the absorption of diffusing species. The second observation is the enlargement of the affected region due to the pressure which leads to more uniform distributions of the chemical quantities.

Results after the diffusion step. After the diffusion takes place, the following result are achieved.

The strains in Fig. 12(a) are different for every model. In case of the M_{TM} submodel, the strain corresponds directly to the temperature depicted in Fig. 12(b). Considering the M_{CM} submodel, a constant elongation is reached. The M_{TCM} model leads to a similar linear distribution as the M_{TM} submodel, but the slope is different as the thermal diffusion induced by the temperature on the lower boundary redistributes the diffusing species.

The pressure in Fig. 13(a) corresponds to the strain in Fig. 12(a). The chemical potentials in Fig. 13(b) vary, though, they should all

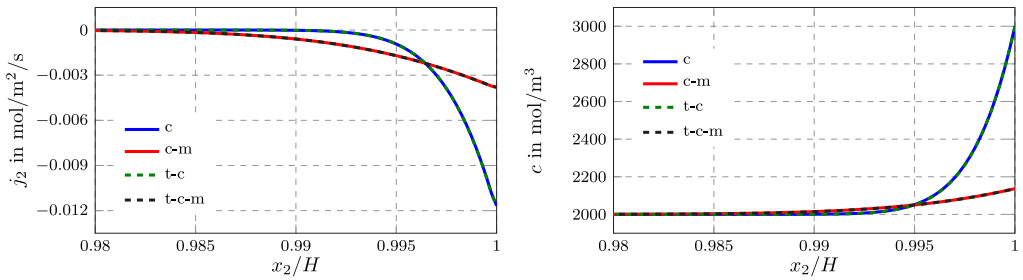

(a) Comparison of fluxes of diffusing species resulting from different models

(b) Comparison of concentrations resulting from different models

Fig. 11. Flux of diffusing species and concentration in an open system at $t = t_{\text{Step1}}$.

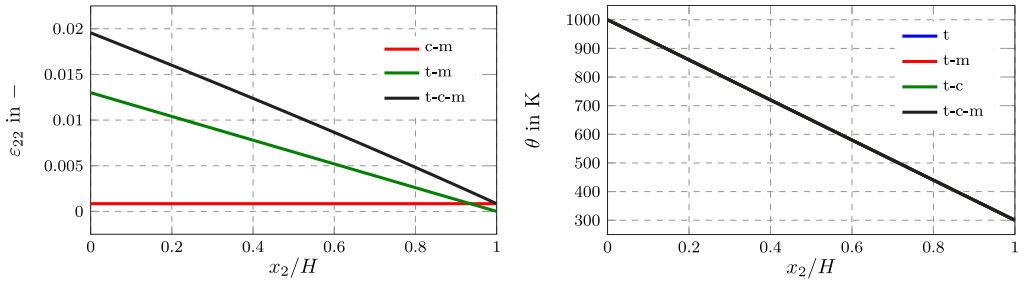

(a) Comparison of longitudinal strains resulting from different models

(b) Comparison of temperatures resulting from different models

Fig. 12. Strain and temperature in an open system at $t = t_{\text{Step2}}$.

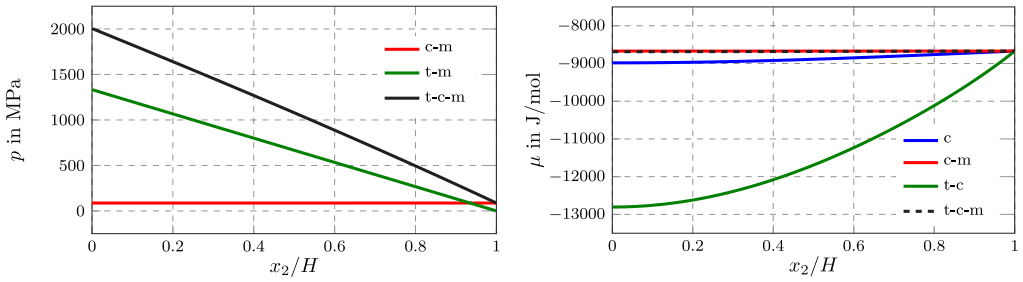

(a) Comparison of pressures resulting from different models

(b) Comparison of chemical potentials resulting from different models

Fig. 13. Pressure and chemical potential in an open system at $t = t_{\text{Step2}}$.

reach the prescribed value of the upper bound. In contrast to the preceding results, the submodels M_C and M_{TC} are not in the equilibrium state. The equilibrium state is defined by the prescribed chemical potential on the upper end. While the pressure induced by the increase of temperature and concentration helps to increase the chemical potential reduced by the temperature, only the concentration itself is able to level out the chemical potential in the M_{TC} submodel.

In Fig. 14(a) fluxes of diffusing species are still active in case the equilibrium state is not reached. In Fig. 14(b) the values at $t = t_{\text{diff}}$ differ in a wide range. The equilibrium concentration of the reference result from the M_C submodel is 3000.0 mol/m^3 while concentration in the M_{CM} submodel remains at around 20% of the expected change. To some extent these solutions bound the concentration of the M_{TCM} model, though the concentration of the M_{TCM} model is slightly higher than 3000.0 mol/m^3 at the lower boundary. The M_{TC} submodel leads to a quite different result as the concentration reaches around 18000.0 mol/m^3 which is six-times the reference result, despite the equilibrium is not achieved yet and, thus, the concentration will reach even higher values.

The open system proves the impact of the temperature on the mechanical and chemical fields as well. The mechanical behavior influences the diffusive behavior especially right on the exposed border and different periods of time are needed in each model to reach an equilibrium state. Especially the mechanical influence accelerates reaching the equilibrium state.

5. Three-dimensional example

5.1. Simulation setup

The results and the comprehension obtained during the preceding study are enrolled on a full-field problem. The preceding study outlines the results which should be expected from the following problem. A circular geometry is considered resembling a pipe, transporting a gaseous phase to which the inner surface of the geometry is exposed

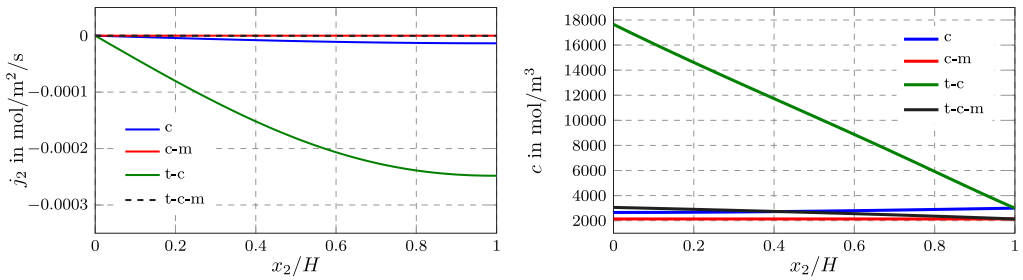

(a) Comparison of fluxes of diffusing species resulting from different models

(b) Comparison of concentrations resulting from different models

Fig. 14. Flux of diffusing species and concentration in an open system at $t = t_{\text{Step2}}$.

to. In Di Leo and Anand (2013) and Chester et al. (2015), similar representations of chemical atmospheres are used. The reduction of the chemical potential represents a heat-up of the gaseous atmosphere interfering with the solid material. Taking the material parameters of a steel-hydrogen pairing into account, an additional pressure prescribed on the inside of the pipe can be neglected for a low hydrogen pressure in the gaseous atmosphere. The pipe is aligned with a temperature gradient such that heat flow and mass flow are in perpendicular directions. The geometry is depicted in Fig. 15 using the symmetry conditions with respect to the Cartesian coordinate system.

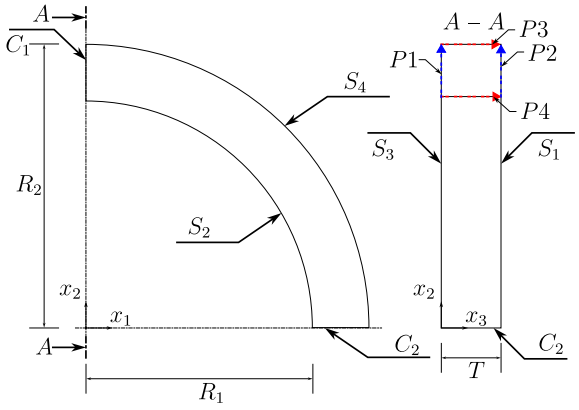

Fig. 15. A cylindrical 3D geometry for a full-field simulation.

Table 3
Geometric dimensions of the circular geometry.

Dimension	Value
R_1	0.3 m
R_2	0.4 m
T	0.1 m

The dimensions of the geometry are listed in Table 3. Surfaces and cutting faces denoted by S and C are depicted in Fig. 15 and referenced in Table 4. The geometry is meshed with 43600 hexahedral elements introduced in the previous section. The initial values are $\mu_0 = -9707.562\,\text{J/mol}$, $\theta_0 = 300.0\,\text{K}$ and $c_0 = 2000.0\,\text{mol/m}^3$, though only two initial values can be chosen independently. The following Dirichlet boundary conditions are applied during a loading step of $t_{\text{Step1}} = 100.0\,\text{s}$ and held constant in a diffusion step of $t_{\text{Step2}} = 8.5 \cdot 10^6\,\text{s}$. The conditions

$$u_1\left(\boldsymbol{x} \in C_1\right) = 0.0\,\text{m},\ u_2\left(\boldsymbol{x} \in C_2\right) = 0.0\,\text{m} \text{ and}$$
$$u_3\left(\boldsymbol{x} \in S_3\right) = 0.0\,\text{m} \tag{64}$$

for the displacement,

$$\mu\left(\boldsymbol{x} \in S_2\right) = \begin{cases} \bar{\mu}\,(t) & t \in t_{\text{Step1}} \\ -16179.27\,\text{J/mol} & t \in t_{\text{Step2}} \end{cases} \tag{65}$$

Table 4
Surface assignment.

Surface flag	Description
C_1	Left cutting face
C_2	Bottom cutting face
S_1	Front surface
S_2	Inner surface
S_3	Back surface
S_4	Outer surface

for the chemical potential and

$$\theta\left(\boldsymbol{x} \in S_3\right) = 300.0\,\text{K} \quad \text{and} \quad \theta\left(\boldsymbol{x} \in S_1\right) = \begin{cases} \bar{\theta}\,(t) & t \in t_{\text{Step1}} \\ 500.0\,\text{K} & t \in t_{\text{Step2}} \end{cases} \tag{66}$$

for the temperature are prescribed. The functions $\bar{\mu}\,(t)$ and $\bar{\theta}\,(t)$ ramp the corresponding fields from their initial values to the values during the diffusion step. The final value of chemical potential on the surface S_2 is calculated using Eq. (37) assuming zero pressure for a concentration of $2000.0\,\text{mol/m}^3$ and a temperature of $500.0\,\text{K}$. Neumann boundary conditions of zero gradients are used on the remaining cutting faces and surfaces for all fields, respectively.

5.2. Comparison to the results of the preceding study

Observations in the preceding study. Due to the preceding study, the following expectations for the equilibrium state after diffusion are set:

- The amount of diffusing species within the solid material will reduce due to the prescribed chemical potential on the surface S_2 leading to a flux of diffusing species pointing to the origin of the coordinate system.
- The temperature gradient between the surfaces S_1 and S_3 will be linear, and a concentration gradient will be induced by the thermodiffusive phenomenon, respectively.
- The stresses near the surface S_3 will be the highest due to the constrained displacement u_3, though near the intersection of the surfaces S_3 and S_4 the concentration will be the lowest leading to a high pressure.

The actual stress state is heavily dependent on the thermo-chemical state as the prescribed temperature leads to a thermal expansion while the prescribed chemical potential induces a contraction.

Discussion on the simulation results. The simulation results are produced using the ABAQUSER tool of Roth et al. (2012). The following figures represent the equilibrium state. In Fig. 15 four plotting paths $P1$–$P4$ around the cutting face $C1$ are marked along which the following results have been evaluated. The solution field is circular such that the following results are valid for the overall geometry. The resulting temperature distribution is linear between the surfaces S_1 and S_3 including a constant gradient directed to the surface S_1.

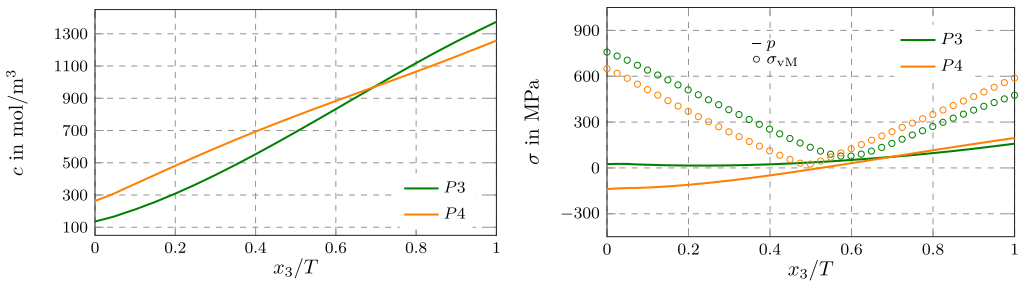

(a) Concentration along $P3$ and $P4$ (b) Stress along $P3$ and $P4$

Fig. 16. Solutions of concentration and stress along $P3$ and $P4$ in the equilibrium state.

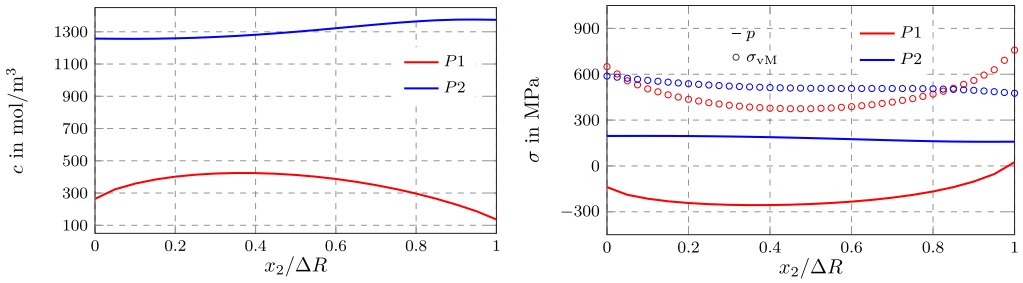

(a) Concentration along $P1$ and $P2$ (b) Stress along $P1$ and $P2$

Fig. 17. Solutions of concentration and stress along $P1$ and $P2$ in the equilibrium state.

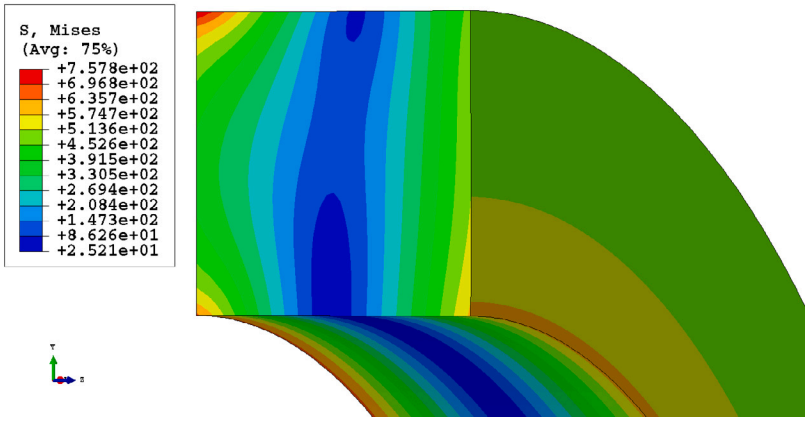

Fig. 18. Contour plot of σ_{vM} in the equilibrium state.

The results for concentration and stress including the pressure and the von Mises stress σ_{vM} along $P3$ and $P4$ are depicted in Fig. 16.

The concentrations depicted in Fig. 16(a) follow the predictions according to the temperature gradient. Nevertheless, the distribution along $P3$ has some variations near the right end leading to higher concentrations than along $P4$. This result corresponds to the pressure depicted in Fig. 16(b). On the left side, the pressure along $P3$ is higher than the one along $P4$ resulting in the difference in concentration in Fig. 16(a). Though, on the right side which represents the hot side, the pressure along $P4$ is higher leading to the higher concentrations along $P3$. Thus, the concentration follows heavily the temperature, but within isothermal regions, the concentration depends on the descending pressure gradient.

The von Mises stress which is a common quantity used in yield functions to represent the stress state, is added in Fig. 16(b). The highest von Mises stresses occur along $P1$ and $P2$ while the center region is hardly touched. The distribution along $P4$ seems to be centered, a horizontal shift to the right of the distribution along the upper boundary is obtained.

The concentrations depicted in Fig. 17(a) change significantly along $P1$ which is the colder side, while the concentration along $P2$ is approximately constant. As these bounds represent paths of isothermal conditions, the concentrations depend mainly on the pressure. Considering Fig. 17(b), the pressure along $P1$ does change significantly as well. The pressure within the center of $P1$ is the lowest, but it increases towards the corners. The pressure $P2$ remains approximately constant within a range of less than 50.0 MPa. Adding the results of the von Mises stress in Fig. 16(b) to the results in Fig. 17(b), the corners on the left side have the highest tendency of yielding due to the highest stress values. In Fig. 18, the contour plot of the von Mises stress in the equilibrium state is depicted. The previous conclusion about the lowest

magnitude in the center is shown as vertical band in the center of the cross-section.

6. Conclusions

The present work deals with a thermo-chemo-mechanically coupled multi-field model using a geometrically linear theory and provides a numerical study on the couplings within this model. The main contributions are:

- The model proposed by Anand (2011) is modified in details and a FE implementation using the UEL subroutine of the ABAQUS Finite Element solver is done. The discretization of the derived set of equations as well as an outline on the general ingredients for the user-defined element is provided supporting the development of further coupled multi-field models.
- A numerical study involving six submodels and the fully coupled thermo-chemo-mechanical model elucidates the capabilities of the presented theory. The study is based on a procedure using ordinary problems to focus on the different results returned by the different models. The study outlines the limits of a geometrically linear theory concerning the chemo-mechanical coupling approximating the conservation of diffusing species, the influence of thermodiffusion and the variation between an activated and a deactivated mechanical dependency at an exposed surface.
- A three-dimensional example provided in the last section demonstrates the supportive character of the study to comprehend the derived multi-field model on the basis of one-dimensional problems. The procedure allows a gradual increase of comprehending the coupled behavior.

CRediT authorship contribution statement

Johannes Gisy: Writing – review & editing, Writing – original draft, Validation, Software, Methodology, Investigation, Formal analysis, Data curation, Conceptualization. **Alexander Dyck:** Writing – review & editing, Formal analysis. **Thomas Böhlke:** Writing – review & editing, Supervision, Resources, Funding acquisition, Conceptualization.

Declaration of competing interest

The authors declare that they have no known competing financial interests or personal relationships that could have appeared to influence the work reported in this paper.

Appendix A. Buildup a user-defined element

As the usage of a UEL subroutine is considered less common, the implementation procedure is explained on a generic field equation first. Considering an arbitrary partial differential equation of second order

$$\dot{Y} = \operatorname{div}(\boldsymbol{\Theta}(Y)) + \xi(Y) \tag{A.1}$$

for the field quantity Y with a nonconvective flux Θ depending on Y and a supply or production ξ depending on Y as well. The strong form in Eq. (A.1) is transformed into its weak form

$$\int_{\mathrm{V}} w_{\mathrm{Y}} \dot{Y} \,\mathrm{d}v = \int_{\mathrm{V}} w_{\mathrm{Y}} \operatorname{div}(\boldsymbol{\Theta}(Y)) \,\mathrm{d}v + \int_{\mathrm{V}} w_{\mathrm{Y}}\, \xi(Y) \,\mathrm{d}v \tag{A.2}$$

by the multiplication of a test function w_{Y} and the integration over the control volume V, (cf. Šilhavý, 1997). The usage of the divergence theorem on the flux reduces the order of this differential equation and leads to

$$0 = \underbrace{\int_{\partial \mathrm{V}} w_{\mathrm{Y}} \bar{\Theta}(Y) \,\mathrm{d}a}_{\text{external forces}} - \underbrace{\left(\int_{\mathrm{V}} w_{\mathrm{Y}} \dot{Y} \,\mathrm{d}v + \int_{\mathrm{V}} \operatorname{grad}(w_{\mathrm{Y}}) \cdot \boldsymbol{\Theta}(Y) \,\mathrm{d}v - \int_{\mathrm{V}} w_{\mathrm{Y}} \xi(Y) \,\mathrm{d}v. \right)}_{\text{internal forces}} \tag{A.3}$$

The order of the resulting terms is external forces minus internal forces recommended in the ABAQUS manual (cf. ABAQUS/Standard, 2020), which guarantees a positive definite element stiffness matrix. The projection of the flux normal to the element surface is $\bar{\Theta}(Y) = \boldsymbol{\Theta}(Y) \cdot \boldsymbol{n}$. Starting from this formulation of the differential equation, discretization schemes can be applied. First, the time is discretized such that the next point in time is calculated by $t^{n+1} = t^n + \Delta t^{n+1}$ with the upcoming increment in time Δt^{n+1}. The starting point $t_0 = 0\,\mathrm{s}$ needs to be known. The rate of Y can be approximated by an implicit Euler scheme

$$\dot{Y} \approx \frac{Y^{n+1} - Y^n}{\Delta t^{n+1}} \tag{A.4}$$

or other discretization schemes. Note, that in general the material time derivative consists of a local contribution and a convective one which is neglected in the present case in accordance to the geometrically linear theory. Secondly, a spatial discretization

$$Y \approx \underline{N}_{\mathrm{Y}}^{\mathrm{T}} \underline{d}_{\mathrm{E,Y}}, \qquad w_{\mathrm{Y}} \approx \underline{N}_{\mathrm{Y}}^{\mathrm{T}} \underline{w}_{\mathrm{E,Y}} \tag{A.5}$$

is introduced using shape functions $\underline{N}_{\mathrm{Y}} \in \mathbb{R}^{N_{\mathrm{N}}}$ which interpolate the nodal values $\underline{d}_{\mathrm{E,Y}}, \underline{w}_{\mathrm{E,Y}} \in \mathbb{R}^{N_{\mathrm{N}}}$ within an element. The shape functions of 8-node linear and 20-node quadratic elements are given in the Appendix B. The usage of the Galerkin FE method enforces identical shape functions for the test function. The gradient of Y is obtained by $\operatorname{grad}(Y) \approx \underline{\boldsymbol{B}}_{\mathrm{Y}}^{\mathrm{T}} \underline{d}_{\mathrm{E,Y}}$ where the B-matrix $\underline{\boldsymbol{B}}_{\mathrm{Y}} \in \mathbb{R}^{N_{\mathrm{N}} \times 3}$ is defined as

$$\underline{\boldsymbol{B}}_{\mathrm{Y}} = \begin{bmatrix} \frac{\partial N_{\mathrm{Y},1}}{\partial x_1} & \frac{\partial N_{\mathrm{Y},1}}{\partial x_2} & \frac{\partial N_{\mathrm{Y},1}}{\partial x_3} \\ \vdots & \vdots & \vdots \\ \frac{\partial N_{\mathrm{Y},N_{\mathrm{N}}}}{\partial x_1} & \frac{\partial N_{\mathrm{Y},N_{\mathrm{N}}}}{\partial x_2} & \frac{\partial N_{\mathrm{Y},N_{\mathrm{N}}}}{\partial x_3} \end{bmatrix}. \tag{A.6}$$

The substitution of the discretized test function into Eq. (A.3) and the specification of the control volume to the volume of one element V_{E} leads to

$$0 = \underline{w}_{\mathrm{E,Y}}^{\mathrm{T}} \underbrace{\left[\int_{\partial \mathrm{V}_{\mathrm{E}}} \underline{N}_{\mathrm{Y}} \bar{\Theta}(Y) \,\mathrm{d}a - \int_{\mathrm{V}_{\mathrm{E}}} \underline{N}_{\mathrm{Y}} \dot{Y} \,\mathrm{d}v - \int_{\mathrm{V}_{\mathrm{E}}} \underline{\boldsymbol{B}}_{\mathrm{Y}} \underline{\Theta}(Y) \,\mathrm{d}v + \int_{\mathrm{V}_{\mathrm{E}}} \underline{N}_{\mathrm{Y}} \xi(Y) \,\mathrm{d}v \right]}_{\underline{R}_{\mathrm{E,Y}}}. \tag{A.7}$$

The flux $\boldsymbol{\Theta}(Y)$ is rewritten using matrix–vector notation and denoted by $\underline{\Theta}(Y)$. For arbitrary test functions, the bracket needs to vanish, thus, an expression for the residual vector is obtained. The element stiffness matrix

$$\begin{aligned} \underline{K}_{\mathrm{E}} = \underline{K}_{\mathrm{E,YY}} &= -\frac{\partial \underline{R}_{\mathrm{E,Y}}}{\partial \underline{d}_{\mathrm{E,Y}}} \\ &= -\int_{\partial \mathrm{V}_{\mathrm{E}}} \frac{\partial \bar{\Theta}(Y)}{\partial Y} \underline{N}_{\mathrm{Y}} \underline{N}_{\mathrm{Y}}^{\mathrm{T}} \,\mathrm{d}a + \int_{\mathrm{V}_{\mathrm{E}}} \frac{\partial \dot{Y}}{\partial Y} \underline{N}_{\mathrm{Y}} \underline{N}_{\mathrm{Y}}^{\mathrm{T}} \,\mathrm{d}v \\ &\quad + \int_{\mathrm{V}_{\mathrm{E}}} \underline{\boldsymbol{B}}_{\mathrm{Y}} \frac{\partial \underline{\Theta}(Y)}{\partial Y} \underline{N}_{\mathrm{Y}}^{\mathrm{T}} \,\mathrm{d}v - \int_{\mathrm{V}_{\mathrm{E}}} \frac{\partial \xi(Y)}{\partial Y} \underline{N}_{\mathrm{Y}} \underline{N}_{\mathrm{Y}}^{\mathrm{T}} \,\mathrm{d}v \end{aligned} \tag{A.8}$$

is the derivative of the residual with respect to the nodal DOF with a negative sign. In Eq. (A.8) a clear separation into a geometrical contribution by the chosen shape functions and a material contribution by the corresponding derivative with respect to Y can be identified. The material contribution is called the material tangent as well. The evaluation of the integrals is done numerically involving quadrature schemes like

$$\int_{\mathrm{V}_{\mathrm{E}}} f(\boldsymbol{x}) \,\mathrm{d}v \approx \sum_{i}^{N_{\mathrm{int}}} f(\boldsymbol{\xi}_i)\, w_i J_{\boldsymbol{\xi} \to \mathbf{x}} \quad \text{and}$$

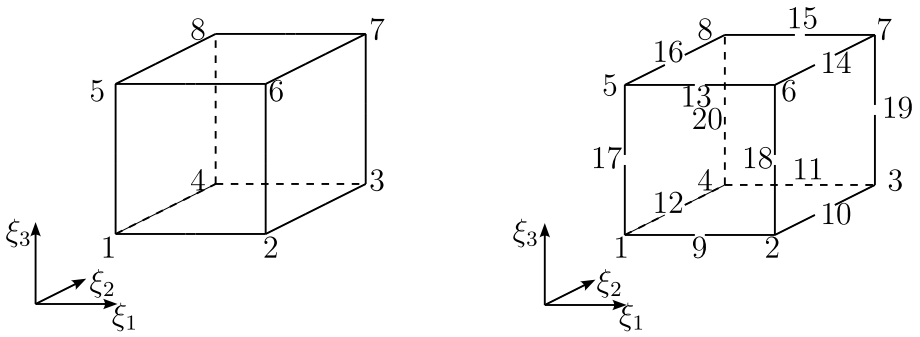

(a) Linear hexahedral element (b) Quadratic hexahedral element

Fig. B.1. Topology and node numbering of the shape functions used.

$$\int_{\partial \mathrm{V_E}} f(\boldsymbol{x})\, \mathrm{d}a \approx \sum_{i}^{N_{\mathrm{S,int}}} f\left(\boldsymbol{\xi}_{\mathrm{S},i}\right) w_{\mathrm{S},i} J_{\mathrm{S},\xi\to\mathbf{x}} \tag{A.9}$$

for the volume and surface integrals, separately. The number of integration points N_{int} and $N_{\mathrm{S,int}}$ as well as their locations $\boldsymbol{\xi}_i$ and $\boldsymbol{\xi}_{\mathrm{S},i}$ and their weights w_i and $w_{\mathrm{S},i}$ need to be defined for both quadratures, respectively. In general, elements are defined in an isoparametric space, thus, the Jacobians $J_{\xi\to\mathbf{x}}$ and $J_{\mathrm{S},\xi\to\mathbf{x}}$ are needed for mapping purposes.

Appendix B. Shape functions

The topology of the linear and quadratic shape functions is depicted in Fig. B.1.

The shape functions given in the isoparametric space $\{\xi_1, \xi_2, \xi_3\}$ are defined as

$$\begin{aligned}
N_1 &= \frac{1}{8}(1-\xi_1)(1-\xi_2)(1-\xi_3)\\
N_2 &= \frac{1}{8}(1+\xi_1)(1-\xi_2)(1-\xi_3)\\
N_3 &= \frac{1}{8}(1+\xi_1)(1+\xi_2)(1-\xi_3)\\
N_4 &= \frac{1}{8}(1-\xi_1)(1+\xi_2)(1-\xi_3)\\
N_5 &= \frac{1}{8}(1-\xi_1)(1-\xi_2)(1+\xi_3)\\
N_6 &= \frac{1}{8}(1+\xi_1)(1-\xi_2)(1+\xi_3)\\
N_7 &= \frac{1}{8}(1+\xi_1)(1+\xi_2)(1+\xi_3)\\
N_8 &= \frac{1}{8}(1-\xi_1)(1+\xi_2)(1+\xi_3)
\end{aligned} \tag{B.1}$$

in case of linear interpolation and

$$\begin{aligned}
N_1 &= -\frac{1}{8}(1-\xi_1)(1-\xi_2)(1-\xi_3)(2+\xi_1+\xi_2+\xi_3)\\
N_2 &= -\frac{1}{8}(1+\xi_1)(1-\xi_2)(1-\xi_3)(2-\xi_1+\xi_2+\xi_3)\\
N_3 &= -\frac{1}{8}(1+\xi_1)(1+\xi_2)(1-\xi_3)(2-\xi_1-\xi_2+\xi_3)\\
N_4 &= -\frac{1}{8}(1-\xi_1)(1+\xi_2)(1-\xi_3)(2+\xi_1-\xi_2+\xi_3)\\
N_5 &= -\frac{1}{8}(1-\xi_1)(1-\xi_2)(1+\xi_3)(2+\xi_1+\xi_2-\xi_3)\\
N_6 &= -\frac{1}{8}(1+\xi_1)(1-\xi_2)(1+\xi_3)(2-\xi_1+\xi_2-\xi_3)\\
N_7 &= -\frac{1}{8}(1+\xi_1)(1+\xi_2)(1+\xi_3)(2-\xi_1-\xi_2-\xi_3)\\
N_8 &= -\frac{1}{8}(1-\xi_1)(1+\xi_2)(1+\xi_3)(2+\xi_1-\xi_2-\xi_3)\\
N_9 &= \frac{1}{4}(1-\xi_1^2)(1-\xi_2)(1-\xi_3) \qquad N_{15} = \frac{1}{4}(1-\xi_1^2)(1+\xi_2)(1+\xi_3)\\
N_{10} &= \frac{1}{4}(1+\xi_1)(1-\xi_2^2)(1-\xi_3) \qquad N_{16} = \frac{1}{4}(1-\xi_1)(1-\xi_2^2)(1+\xi_3)\\
N_{11} &= \frac{1}{4}(1-\xi_1^2)(1+\xi_2)(1-\xi_3) \qquad N_{17} = \frac{1}{4}(1-\xi_1)(1-\xi_2)(1-\xi_3^2)\\
N_{12} &= \frac{1}{4}(1-\xi_1)(1-\xi_2^2)(1-\xi_3) \qquad N_{18} = \frac{1}{4}(1+\xi_1)(1-\xi_2)(1-\xi_3^2)\\
N_{13} &= \frac{1}{4}(1-\xi_1^2)(1-\xi_2)(1+\xi_3) \qquad N_{19} = \frac{1}{4}(1+\xi_1)(1+\xi_2)(1-\xi_3^2)\\
N_{14} &= \frac{1}{4}(1+\xi_1)(1-\xi_2^2)(1+\xi_3) \qquad N_{20} = \frac{1}{4}(1-\xi_1)(1+\xi_2)(1-\xi_3^2)
\end{aligned} \tag{B.2}$$

in case of quadratic interpolation.

Appendix C. Element tangents

The derivatives of the chemical potential are

$$\frac{\partial \hat{\mu}}{\partial \boldsymbol{\epsilon}} = -K_0 \Omega_0 \boldsymbol{I}, \tag{C.1}$$

$$\frac{\partial \hat{\mu}}{\partial c} = \frac{R\theta}{c\left(1-c_{\mathrm{n}}\right)} + K_0 \Omega_0^2 \tag{C.2}$$

and

$$\frac{\partial \hat{\mu}}{\partial \theta} = R \ln\left(\frac{c_{\mathrm{n}}}{1-c_{\mathrm{n}}}\right) + 3K_0 \alpha_0 \Omega_0. \tag{C.3}$$

Using these relations to calculate the derivates of the concentration, the following formulations are obtained

$$\frac{\partial \hat{c}}{\partial \mu} = \left(\frac{R\theta}{c\left(1-c_{\mathrm{n}}\right)} + K_0 \Omega_0^2\right)^{-1}, \tag{C.4}$$

$$\frac{\partial \hat{c}}{\partial \boldsymbol{\epsilon}} = K_0 \Omega_0 \left(\frac{R\theta}{c\left(1-c_{\mathrm{n}}\right)} + K_0 \Omega_0^2\right)^{-1} \boldsymbol{I} \tag{C.5}$$

and

$$\frac{\partial \hat{c}}{\partial \theta} = -\left(R \ln\left(\frac{c_{\mathrm{n}}}{1-c_{\mathrm{n}}}\right) + 3K_0 \alpha_0 \Omega_0\right)\left(\frac{R\theta}{c\left(1-c_{\mathrm{n}}\right)} + K_0 \Omega_0^2\right)^{-1}. \tag{C.6}$$

The second order derivative needed is

$$\frac{\partial^2 \hat{\mu}}{\partial \theta \partial c} = \frac{R}{c\left(1-c_{\mathrm{n}}\right)} \tag{C.7}$$

The thermal stress coefficient reads

$$\frac{\partial \hat{\boldsymbol{\sigma}}}{\partial \theta} = -3K_0 \alpha_0 \boldsymbol{I}. \tag{C.8}$$

Further derivates of the stress are

$$\frac{\partial \hat{\boldsymbol{\sigma}}}{\partial \boldsymbol{\epsilon}} = 3K_0 \mathbb{P}_1 + 2G_0 \mathbb{P}_2 \tag{C.9}$$

and

$$\frac{\partial \hat{\boldsymbol{\sigma}}}{\partial c} = -K_0 \Omega_0 \boldsymbol{I}. \tag{C.10}$$

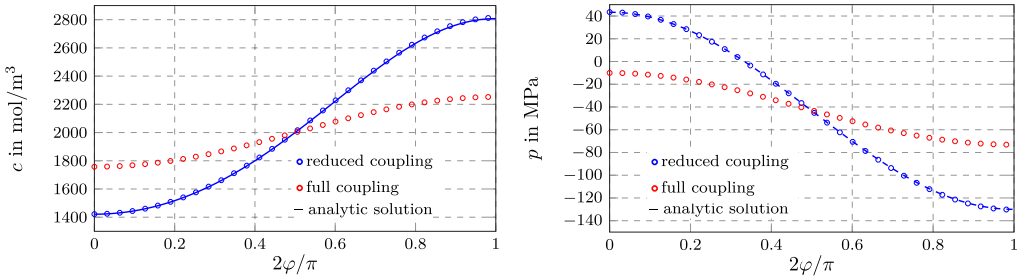

(a) Comparison of concentrations calculated analytically and numerically

(b) Comparison of pressure calculated analytically and numerically

Fig. D.1. Numerical and analytical solutions for a full and reduced chemo-mechanical problem on the notched plate.

The rate of concentrations is

$$\dot{c} = \left(\frac{R\theta}{c\,(1-c_\mathrm{n})} + K_0\Omega_0^2 \right)^{-1} \left(\dot{\mu} + K_0\Omega_0 \mathrm{tr}\,(\dot{\boldsymbol{\varepsilon}}) - \left(R \ln\left(\frac{c_\mathrm{n}}{1-c_\mathrm{n}} \right) + 3K_0\alpha_0\Omega_0 \right) \dot{\theta} \right). \tag{C.11}$$

The derivates of the rate of concentrations follow with

$$\frac{\partial \hat{\dot{c}}}{\partial \mu} = -\left(\frac{R\theta}{c\,(1-c_\mathrm{n})} + K_0\Omega_0^2 \right)^{-2} \frac{R}{c\,(1-c_\mathrm{n})} \left(\frac{2c_\mathrm{n}-1}{c\,(1-c_\mathrm{n})} \theta\dot{c} + \dot{\theta} \right) + \left(\frac{R\theta}{c\,(1-c_\mathrm{n})} + K_0\Omega_0^2 \right)^{-1} \frac{1}{\Delta t}, \tag{C.12}$$

$$\frac{\partial \hat{\dot{c}}}{\partial \boldsymbol{\varepsilon}} = -\left(\frac{R\theta}{c\,(1-c_\mathrm{n})} + K_0\Omega_0^2 \right)^{-2} \frac{RK_0\Omega_0 \boldsymbol{I}}{c\,(1-c_\mathrm{n})} \left(\frac{2c_\mathrm{n}-1}{c\,(1-c_\mathrm{n})} \theta\dot{c} + \dot{\theta} \right) + \left(\frac{R\theta}{c\,(1-c_\mathrm{n})} + K_0\Omega_0^2 \right)^{-1} \frac{K_0\Omega_0 \boldsymbol{I}}{\Delta t}, \tag{C.13}$$

and

$$\frac{\partial \hat{\dot{c}}}{\partial \theta} = \left(R \ln\left(\frac{c_\mathrm{n}}{1-c_\mathrm{n}} \right) + 3K_0\alpha_0\Omega_0 \right) \left(\frac{R\theta}{c\,(1-c_\mathrm{n})} + K_0\Omega_0^2 \right)^{-2} \frac{R}{c\,(1-c_\mathrm{n})} \left(\frac{2c_\mathrm{n}-1}{c\,(1-c_\mathrm{n})} \theta\dot{c} + \dot{\theta} \right) - \left(\frac{R\theta}{c\,(1-c_\mathrm{n})} + K_0\Omega_0^2 \right)^{-1} \left(\left(R \ln\left(\frac{c_\mathrm{n}}{1-c_\mathrm{n}} \right) + 3K_0\alpha_0\Omega_0 \right) \frac{1}{\Delta t} + \frac{R\dot{c}}{c\,(1-c_\mathrm{n})} \right). \tag{C.14}$$

The derivatives of the flux of diffusing species are

$$\frac{\partial \hat{\boldsymbol{j}}}{\partial c} = -\frac{D_0}{R\theta} \left(1 - 2c_\mathrm{n} \right) \boldsymbol{m}, \tag{C.15}$$

$$\frac{\partial \hat{\boldsymbol{j}}}{\partial \boldsymbol{m}} = -\frac{D_0}{R\theta} c\,(1-c_\mathrm{n})\, \boldsymbol{I} \tag{C.16}$$

and

$$\frac{\partial \hat{\boldsymbol{j}}}{\partial \theta} = \frac{D_0}{R\theta^2} c\,(1-c_\mathrm{n})\, \boldsymbol{m}. \tag{C.17}$$

The derivative of the heat flux is

$$\frac{\partial \hat{\boldsymbol{q}}}{\partial \boldsymbol{g}} = -\kappa_0. \tag{C.18}$$

Appendix D. Validation of the chemo-mechanical coupling

The displacement and the chemical potential at isothermal conditions are considered. In general, the analytical solution on such a two-field problem is still not available, thus, the chemical strain is neglected such that the stress depends on the displacement gradient only. In Barrera et al. (2016) such a two-field problem is considered for a notched plate where the chosen geometry enables an analytical solution for the heterogeneous stress state right at the notch in case for unidirectional loading. A similar setting is used in Villani et al. (2014) as well to compare different models. The solution for the stress depending on the applied load σ_0 is well-documented (cf. Anand and Govindjee, 2020). At a sufficient distance from the notch, the chemical potential homogeneous is assumed unchanged, and the stress is constant such that the concentration remains at its initial value. This assumption leads to

$$c\,(\varphi) = \frac{be^a}{be^a+1} c_\mathrm{max} \quad \text{with} \quad a = -\frac{2\Omega_0\sigma_0\,(1+\nu_0)\cos(2\varphi)}{3R\theta} \quad \text{and} \quad b = \frac{c_0}{(c_\mathrm{max}-c_0)} \tag{D.1}$$

for the concentration along right at the notch. The position right at the notch is described by the polar coordinate φ. The presented model is adapted such that Eqs. (38) and (43) are solved for isothermal conditions at $\theta_0 = 300.0\,\mathrm{K}$ and a vanishing strain decomposition. One fourth of the notched plate is considered with an edge length of $L = 0.5\,\mathrm{m}$ and a notch radius of $r = 0.005\,\mathrm{m}$. The geometry is meshed using 14223 elements. The initial conditions are $c_0 = 2000.0\,\mathrm{mol/m^3}$ and $\mu_0 = -9707.562\,\mathrm{J/mol}$, respectively. A plane strain state is considered such that $u_3 = 0.0\,\mathrm{m}$. Symmetry conditions for the displacement are used on the cutting faces. The concentration is sealed on all bounds. In a first step, a unidirectional load of $\sigma_0 = 100.0\,\mathrm{MPa}$ is ramped up during a period of time of $t_\mathrm{load} = 1000.0\,\mathrm{s}$. In a second step, the load remains constant and diffusion takes place during a period of time of $t_\mathrm{diff} = 5.0 \cdot 10^6\,\mathrm{s}$. The automatic incrementation is used as described in Section 3. Using the material parameters listed in Table D.5, the following solutions in Fig. D.1 for the pressure and the concentration are obtained in the equilibrium state.

In Fig. D.1(a), the concentrations obtained analytically and numerically for the reduced coupling and the full coupling are shown. In case of the reduced coupling, the numerical solution matches the analytical solution. Taking the full coupling into account, the redistribution of the concentration is less significant. Similar results are obtained for the pressure in Fig. D.1(b). The numerical solution is identical to the analytical solution in case of a reduced coupling. Taking the chemical strain into account in the fully coupled simulation, the magnitude of the pressure is reduced overall.

Table D.5
Material parameters for an analytical comparison.

Parameter	Value
E_0	200.0 GPa
ν_0	0.3
$\widetilde{\mu}$	0.0 J mol^{-1}
R	8.3145 J mol^{-1} K^{-1}
Ω_0	$1.0 \cdot 10^{-5}$ m^3 mol^{-1}
$c_{\max}$	$1.0 \cdot 10^{5}$ mol m^{-3}
D_0	$1.0 \cdot 10^{-8}$ m^2 s^{-1}

Data availability

Data will be made available on request.

References

ABAQUS/Standard, 2020. ABAQUS/Standard User's Manual, Version 2020. Dassault Systèmes Simulia Corp., Providence, RI.

Afshar, A., Di Leo, C.V., 2021. A thermodynamically consistent gradient theory for diffusion–reaction–deformation in solids: Application to conversion-type electrodes. J. Mech. Phys. Solids 151, http://dx.doi.org/10.1016/J.JMPS.2021.104368.

Anand, L., 2011. A thermo-mechanically-coupled theory accounting for hydrogen diffusion and large elastic–viscoplastic deformations of metals. Int. J. Solids Struct. 48, 962–971. http://dx.doi.org/10.1016/J.IJSOLSTR.2010.11.029.

Anand, L., 2012. A Cahn–Hilliard-type theory for species diffusion coupled with large elastic–plastic deformations. J. Mech. Phys. Solids 60, 1983–2002. http://dx.doi.org/10.1016/j.jmps.2012.08.001.

Anand, L., Govindjee, S., 2020. Continuum Mechanics of Solids, vol. 62, Oxford University PressOxford, http://dx.doi.org/10.1093/oso/9780198864721.001.0001.

Anguiano, M., Masud, A., Rajagopal, K.R., 2022. Mixture model for thermo-chemo-mechanical processes in fluid-infused solids. Internat. J. Engrg. Sci. 174, 103576. http://dx.doi.org/10.1016/j.ijengsci.2021.103576.

Barrera, O., Tarleton, E., Tang, H., Cocks, A., 2016. Modelling the coupling between hydrogen diffusion and the mechanical behaviour of metals. Comput. Mater. Sci. 122, 219–228. http://dx.doi.org/10.1016/j.commatsci.2016.05.030.

Bistri, D., Di Leo, C.V., 2023. A continuum electro-chemo-mechanical gradient theory coupled with damage: Application to Li-metal filament growth in all-solid-state batteries. J. Mech. Phys. Solids 174, http://dx.doi.org/10.1016/J.JMPS.2023.105252.

Bower, A.F., Guduru, P.R., Sethuraman, V.A., 2011. A finite strain model of stress, diffusion, plastic flow, and electrochemical reactions in a lithium-ion half-cell. J. Mech. Phys. Solids 59, 804–828. http://dx.doi.org/10.1016/J.JMPS.2011.01.003.

Chester, S.A., Di Leo, C.V., Anand, L., 2015. A finite element implementation of a coupled diffusion-deformation theory for elastomeric gels. Int. J. Solids Struct. 52, 1–18. http://dx.doi.org/10.1016/j.ijsolstr.2014.08.015.

Coleman, B.D., Gurtin, M.E., 1967. Thermodynamics with internal state variables. J. Chem. Phys. 47, 597–613. http://dx.doi.org/10.1063/1.1711937.

Coleman, B.D., Noll, W., 1963. The thermodynamics of elastic materials with heat conduction and viscosity. Arch. Ration. Mech. Anal. 13, 167–178. http://dx.doi.org/10.1007/BF01262690.

de Groot, S.R., Mazur, P., 1984. Non-equilibrium Thermodynamics. Dover Publications, New York, p. 510.

DeHoff, R., 2006. Thermodynamics in Materials Science. CRC Press, Boca Raton, http://dx.doi.org/10.1201/9781420005851.

Di Leo, C.V., Anand, L., 2013. Hydrogen in metals: A coupled theory for species diffusion and large elastic–plastic deformations. Int. J. Plast. 43, 42–69. http://dx.doi.org/10.1016/j.ijplas.2012.11.005.

Di Leo, C.V., Rejovitzky, E., Anand, L., 2015. Diffusion-deformation theory for amorphous silicon anodes: The role of plastic deformation on electrochemical performance. Int. J. Solids Struct. 67–68, 283–296. http://dx.doi.org/10.1016/j.ijsolstr.2015.04.028.

Fish, J., Belytschko, T., 2007. A First Course in Finite Elements. Wiley, Chichester, UK, pp. 1–319. http://dx.doi.org/10.1002/9780470510858.

Fried, E., Gurtin, M.E., 1999. Coherent solid-state phase transitions with atomic diffusion: A thermomechanical treatment. J. Stat. Phys. 95, 1361–1427. http://dx.doi.org/10.1023/A:1004535408168/METRICS.

Greve, R., 2003. Kontinuumsmechanik. Springer Berlin Heidelberg, Berlin, Heidelberg, http://dx.doi.org/10.1007/978-3-642-55485-8.

Gurtin, M.E., Fried, E., Anand, L., 2010. The Mechanics and Thermodynamics of Continua. Cambridge University Press, http://dx.doi.org/10.1017/CBO9780511762956.

Gurtin, M.E., Vargas, A.S., 1971. On the classical theory of reacting fluid mixtures. Arch. Ration. Mech. Anal. 43, 179–197. http://dx.doi.org/10.1007/BF00251451/METRICS.

Helnwein, P., 2001. Some remarks on the compressed matrix representation of symmetric second-order and fourth-order tensors. Comput. Methods Appl. Mech. Engrg. 190, 2753–2770. http://dx.doi.org/10.1016/S0045-7825(00)00263-2.

Johlitz, M., Lion, A., 2013. Chemo-thermomechanical ageing of elastomers based on multiphase continuum mechanics. Contin. Mech. Thermodyn. 25, 605–624. http://dx.doi.org/10.1007/s00161-012-0255-8.

Lion, A., Johlitz, M., 2020. On the thermomechanics of solids surrounded by liquid media: balance equations, free energy and nonlinear diffusion. Contin. Mech. Thermodyn. 32, 281–305. http://dx.doi.org/10.1007/s00161-019-00828-5.

Loeffel, K., Anand, L., 2011. A chemo-thermo-mechanically coupled theory for elastic-viscoplastic deformation, diffusion, and volumetric swelling due to a chemical reaction. Int. J. Plast. 27, 1409–1431. http://dx.doi.org/10.1016/J.IJPLAS.2011.04.001.

Meixner, J., Reik, H.G., 1959. Thermodynamik der irreversiblen prozesse. In: Flügge, S. (Ed.), Prinzipien der Thermodynamik und Statistik. Springer Berlin Heidelberg, Berlin, Heidelberg, pp. 413–523. http://dx.doi.org/10.1007/978-3-642-45912-2_4,

Mianroodi, J.R., Shanthraj, P., Liu, C., Vakili, S., Roongta, S., Siboni, N.H., Perchikov, N., Bai, Y., Svendsen, B., Roters, F., Raabe, D., Diehl, M., 2022. Modeling and simulation of microstructure in metallic systems based on multi-physics approaches. npj Comput. Mater. 8, 93. http://dx.doi.org/10.1038/s41524-022-00764-0.

Müller, I., 1985. Thermodynamics. In: Interaction of mechanics and mathematics series, Pitman Advanced Publ. Program, Boston [u.a.].

Neumann, R., Böhlke, T., 2016. Hashin-Shtrikman type mean field model for the two-scale simulation of the thermomechanical processing of steel. Int. J. Plast. 77, 1–29. http://dx.doi.org/10.1016/j.ijplas.2015.09.003.

Oskay, C., 2012. Variational multiscale enrichment for modeling coupled mechano-diffusion problems. Internat. J. Numer. Methods Engrg. 89, 686–705. http://dx.doi.org/10.1002/NME.3258.

Oskay, C., Haney, M., 2010. Computational modeling of titanium structures subjected to thermo-chemo-mechanical environment. Int. J. Solids Struct. 47, 3341–3351. http://dx.doi.org/10.1016/J.IJSOLSTR.2010.08.014.

Qin, B., Zhong, Z., 2021. A theoretical model for thermo-chemo-mechanically coupled problems considering plastic flow at large deformation and its application to metal oxidation. Int. J. Solids Struct. 212, 107–123. http://dx.doi.org/10.1016/J.IJSOLSTR.2020.12.006.

Rahman, M.A., Saghir, M.Z., 2014. Thermodiffusion or soret effect: Historical review. Int. J. Heat Mass Transfer 73, 693–705. http://dx.doi.org/10.1016/J.IJHEATMASSTRANSFER.2014.02.057.

Roth, S., Hütter, G., Mühlich, U., Nassauer, B., Zybell, L., Kuna, M., 2012. Visualisation of user defined finite elements with Abaqus/Viewer. GACM Rep. 7–14.

Šilhavý, M., 1997. The Mechanics and Thermodynamics of Continuous Media. Springer Berlin Heidelberg, Berlin, Heidelberg, http://dx.doi.org/10.1007/978-3-662-03389-0.

Villani, A., Busso, E.P., Ammar, K., Forest, S., Geers, M.G., 2014. A fully coupled diffusional-mechanical formulation: numerical implementation, analytical validation, and effects of plasticity on equilibrium. Arch. Appl. Mech. 84, 1647–1664. http://dx.doi.org/10.1007/S00419-014-0860-Z/METRICS.